

**This is an electronic reprint of the original article.
This reprint *may differ* from the original in pagination and typographic detail.**

Author(s): Honkala, Karoliina

Title: Tailoring oxide properties: An impact on adsorption characteristics of molecules and metals

Year: 2014

Version:

Please cite the original version:

Honkala, K. (2014). Tailoring oxide properties: An impact on adsorption characteristics of molecules and metals. *Surface Science Reports*, 69(4), 366-388.
<https://doi.org/10.1016/j.surfrep.2014.09.002>

All material supplied via JYX is protected by copyright and other intellectual property rights, and duplication or sale of all or part of any of the repository collections is not permitted, except that material may be duplicated by you for your research use or educational purposes in electronic or print form. You must obtain permission for any other use. Electronic or print copies may not be offered, whether for sale or otherwise to anyone who is not an authorised user.

Tailoring oxide properties: an impact on adsorption characteristics of molecules and metals

K. Honkala¹

*¹Department of Chemistry, Nanoscience Center, P.O. Box 35,
University of Jyväskylä, FIN-40014 Jyväskylä, Finland*

(Dated: September 12, 2014)

Abstract

Both density functional theory calculations and numerous experimental studies demonstrate a variety of unique features in metal supported oxide films and transition metal doped simple oxides, which are markedly different from their unmodified counterparts. This review highlights, from the computational perspective, recent literature on the properties of the above mentioned surfaces and how they adsorb and activate different species, support metal aggregates, and even catalyse reactions. The adsorption of Au atoms and clusters on metal-supported MgO films are reviewed together with the cluster's theoretically predicted ability to activate and dissociate O₂ at the Au-MgO(100)/Ag(100) interface, as well as the impact of an interface vacancy to the binding of an Au atom. In contrast to a bulk MgO surface, an Au atom binds strongly on a metal-supported ultra-thin MgO film and becomes negatively charged. Similarly, Au clusters bind strongly on a supported MgO(100) film and are negatively charged favouring 2D planar structures. The adsorption of other metal atoms is briefly considered and compared to that of Au. Existing computational literature of adsorption and reactivity of simple molecules including O₂, CO, NO₂, and H₂O on mainly metal-supported MgO(100) films is discussed. Chemical reactions such as CO oxidation and O₂ dissociation are discussed on the bare thin MgO film and on selected Au clusters supported on MgO(100)/metal surfaces. The Au atoms at the perimeter of the cluster are responsible for catalytic activity and calculations predict that they facilitate dissociative adsorption of oxygen even at ambient conditions. The interaction of H₂O with a flat and stepped Ag-supported MgO film is summarized and compared to bulk MgO. The computational results highlight spontaneous dissociation on MgO steps. Furthermore, the impact of water coverage on adsorption and dissociation is addressed. The modifications, such as oxygen vacancies and dopants, at the oxide-metal interface and their effect on the adsorption characteristics of water and Au are summarized. Finally, more limited computational literature on transition metal (TM) doped CaO(100) and MgO(100) surfaces is presented. Again, Au is used as a probe species. Similar to metal-supported MgO films, Au binds more strongly than on undoped CaO(100) and becomes negatively charged. The discussion focuses on rationalization of Au adsorption with the help of Born-Haber cycle, which reveals that the so called redox energy including the electron transfer from the dopant to the Au atom together with the simultaneous structural relaxation of lattice atoms is responsible for enhanced binding. In addition, adsorption energy dependence on the position and type of the dopant is summarized.

PACS numbers:

I. INTRODUCTION

Metal oxides have long been considered as potential materials for large variety of applications ranging from gas sensing and protective coatings to electrodes in fuel cells, heterogeneous photo(electro) catalyst, and bio-compatible materials¹. Compared to any other material class both crystallographic and electronic properties of oxides display diverse behaviour, e.g., electronic conductivity ranges from wide-gap insulators to materials with conductivity comparable to metals². The characteristics of oxides can be tailored to improve desired properties in various ways by introducing structural modifications like steps and grain boundaries, adding impurity atoms as dopants, or removing atoms from the structure^{1,2}. In particular, point defects such as oxygen vacancies determine optical, electronic and transport properties of insulating oxides, and they usually dominate the chemistry of its surface³. While transition metal oxides are utilized for their catalytic properties, simple oxides such as MgO or CaO are intrinsically inert owing to their very deep valence band and very high conduction band; thus, they are less exploited in applications. However, simple oxides are interesting model systems whose properties have been thoroughly investigated^{1,4} and therefore they form an ideal platform to explore the impact of different tailoring strategies to improve their reactivity. One way to achieve this is to prepare oxides as metal grown thin films, which provides an unique approach to modify structural, electronic and chemical properties as a function of film thickness extensively, which is discussed in the reviews of Prof. H.J. Freund, Prof. G. Pacchioni, and Prof. N. Nilius⁵⁻⁸. From the experimental point of view metal supported thin-film systems create specific technical challenges to be tackled. The significant benefit of ultra-thin arrangement of insulating oxides is that they can be studied with scanning tunneling microscopy (STM), which is not possible for their bulk counterparts. Ultra-thin oxide films such as MgO^{6,9}, NiO¹⁰, CaO¹¹, Al₂O₃^{12,13}, FeO¹⁴⁻¹⁶, and SiO₂¹⁷ have been extensively studied. A comprehensive overview of metal-supported transition metal oxide films can be found in reference¹⁸. Possible applications of metal supported ultra-thin oxide films can be divided into two groups: support materials and active players in chemical conversions. Gold clusters on metal supported ultra-thin films show distinct features compared to clusters on bulk films⁵ and calculations predict that the perimeter of these particles is highly reactive e.g., activating oxygen readily¹⁹. Supported films can also directly act as a catalyst for CO oxidation^{20,21} and dissociate H₂²². Furthermore, metal-supported ultra-thin

films are reactive towards water dissociation²³.

Other ultra-thin insulating materials grown on metal surfaces include e.g., NaCl on Cu(111), which is used as a substrate to explore charge transport to nanostructures including Au adatoms²⁴⁻²⁶. While the stoichiometry and atomic structure of ultra-thin MgO corresponds that of the bulk MgO, this is not always the case. The most prominent example of this is an ultra-thin alumina film over a NiAl support for which determination of atomic structure turned out to be particularly challenging owing to a complex atomic structure. From the interplay between STM experiments and density functional theory (DFT) calculations, the peculiar alumina structure was revealed and it corresponds to Al₁₀O₁₃ being oxygen deficient with respect to bulk Al₂O₃¹². Recently, the studies on thin film systems have extended to solid oxide solution thin films on a metal substrate. In the case of NiO-MgO/Mo it was found that the metal support increases the relative stability of the Ni solute at the oxide film²⁷.

Both experiments and calculations show that metal substrate grown thin oxide layers introduce variable new phenomena. First and foremost charge transfer between electronegative adsorbates such as O₂ and Au, and an oxide-metal interface is generally found to significantly activate an adsorbate and it depends on the film thickness⁸. The occurrence of charge transfer to an Au atom on a Ag-supported MgO film was first predicted by DFT computations²⁸. The charge transfer was verified by employing STM measurements to analyse the samples containing Au atoms deposited on a MgO(3ML)/Ag(100) surface at low coverage and temperature²⁹. The results highlight the formation of ordered Au adsorption structures owing to charge transfer from the substrate. This picture can be further complicated by the presence of defects and low coordinated sites. The substrate's response to a charged adsorbate comprises the relaxation of lattice atoms near an adsorption site to accommodate the extra charge³⁰. Film thickness also affects the metal-oxide interface adhesion, which can be further modified by suitable transition metal dopants³¹.

An alternative approach to modify the properties of oxides is to introduce dopant atoms into a host oxide. This can be achieved by replacing a small fraction of the cations in an oxide with different guest cations. Dopants modify the electronic structure and chemical characteristics of an oxide³² via exchanging electrons with host oxides and adsorbed species. However, dopant atoms can have either lower or higher valence compared to a cation they substitute and this dictates their impact on host oxide characteristics. In the latter case, the

influence of a dopant resembles that of a metal support in the ultra-thin oxide film. However, the number of spare electrons depends on the concentration of dopants and the fact that the dopants can be mobile, unlike the metal support. There is a large body of studies, where the impact of substitutional doping on catalytic properties of oxides has been examined for example see references in^{32,33}. In many cases it has been shown that the reactivity has improved upon doping. Among the studied systems Li-doped MgO has received the most attention owing to its use as a catalyst for oxidative methane coupling to ethane that is often labeled as Holy Grail in catalysis³⁴⁻³⁶. Despite extensive research on this topic, many questions have remained open, and there is not a conclusive understanding of the role of the catalyst, let alone its structure. In the case of CaO, STM studies demonstrate that tiny amounts of Mo embedded into the oxide introduce similar features as metal-supported ultra-thin MgO films namely, Au atoms become negatively charged^{37,38} and Au aggregates favour the 2D growth mode³⁹. Calculations predict enhanced binding of Au adatoms, which is due to electron transfer from Mo to the adsorbate and substantial lattice relaxations near the dopant originating from increased attraction between more positively charged Mo and surrounding anions⁴⁰. Notwithstanding the similarities, TM-doped simple oxides and metal-supported ultra-thin oxide systems show fundamental differences as impact of dopant is more localised compared to metal support, and a number of electrons that the dopant can provide is very limited, which means that the dopant concentration is a new adjustable parameter.

II. PREPARATION AND PROPERTIES OF MODIFIED SIMPLE OXIDES

Here the preparation of oxide systems is briefly discussed and for a more detailed discussion on the preparation and experimental studies of ultra-thin films and simple doped oxides refer to previous reviews^{5,6,8}. Ultra-thin-oxide layers are synthesized by the vaporization of metals such as Mg in a background of molecular oxygen on a metal support and they typically have smaller optimal lattice parameters than bulk oxides⁴¹. By far the most extensively studied ultra-thin oxide film is MgO for which the best support is either a Ag(100) or Mo(100) surface owing to small lattice mismatch, which amounts to 3% and 5.4 %, for Ag and Mo respectively. In the thin film structure O anions are preferably located above Ag/Mo atoms⁴² as displayed in Figure 1. Already a 3ML-thick MgO film on a Ag-support

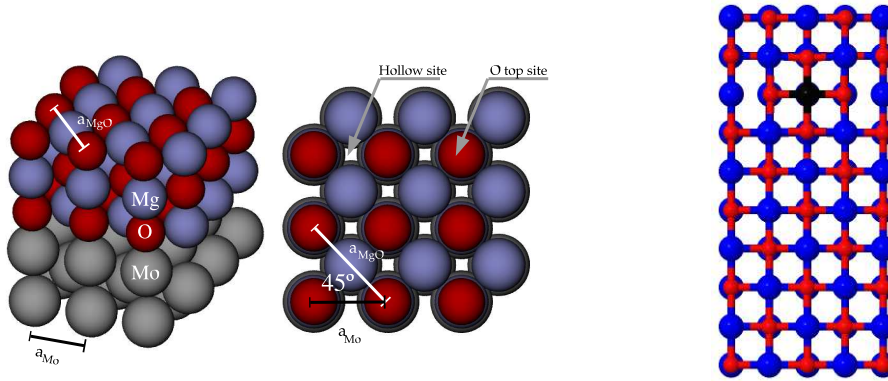


FIG. 1: Left: The side and top view of the 3ML thick MgO(100) film on a Mo(100) surface. The size of the computational surface unit cell is (3x3), and a_{Mo} and a_{MgO} correspond to the lattice parameters of Mo and MgO, respectively⁴³. Right: The side view of a 10 ML thick CaO slab with a dopant cation in the third layer. Atomic color codes: blue (Mg), red (O), and black (dopant).

is sufficient to reproduce the band gap of bulk MgO⁹.

Crucial to the characteristics of metal-supported ultra-thin oxide materials is the interaction between a metal substrate and an oxide film, which affects both the geometric and electronic properties of the system. Furthermore, even a small lattice mismatch, like the one for MgO/Mo, introduces strain effects into the oxide during the film growth. This leads to substantial lattice relaxations and formation of complex network of abundant dislocation lines as demonstrated by STM experiments^{44,45}. They are not only important for film morphology but drastically modify the electronic structure since they are rich in point defects and impurities, and able to trap substantial amount of excess charges. To the best of my knowledge, no computational studies exist for understanding dislocation lines in thin films systems. Theoretical studies for bulk MgO demonstrates the importance of electron trapping in extended defects⁴⁶.

Calculations show that MgO layers attach loosely to the Ag(100) surface, whereas the interaction between the regular MgO and Mo is stronger, owing to larger covalency contribution of the oxygen anions and Mo^{28,42,47}. This is seen in calculated MgO-metal distances, which are shorter for MgO-Mo than for MgO-Ag systems^{28,48}. The existing experimental data indicates that MgO-Ag distance varies between 2.37 Å and 2.53 Å⁴⁹⁻⁵¹. The calculated equilibrium MgO-metal distance depends naturally on the substrate metal, and the choice of

the exchange correlation functional. While PBE and RPBE functionals tend to exaggerate the MgO-metal distance⁵², the inclusion of van der Waals interactions reduces the MgO-Ag distance to 2.5 Å⁵², which is in line with experiments^{49,50}. For a single MgO layer calculations give 0.2 (0.1) Å rumpling (either cations or anions are closer to the metal surface) on a Mo(Ag) support^{42,48} but already in a bilayer system rumpling drops substantially being only 0.1 Å for the Mo support. The detailed analysis of the MgO-metal interface attributed rumpling to a structural response to the interfacial charge transfer and formation of the interfacial dipole⁵³.

Structural characteristics at the interface impact strongly on electronic properties of a system, which is seen as changes in work function of support metal studied extensively both experimentally⁵⁴⁻⁵⁶ and theoretically⁵⁷⁻⁵⁹. Three different factors are identified to be responsible for observed changes owing to presence of the ultra-thin oxide film^{59,60}. These include (i) the suppression of electron density spillover from the metal due to Coulomb repulsion by anions in oxide, which depends on the oxide-metal distance, (ii) charge transfer from oxide (metal) to metal (oxide), and (iii) interfacial rumpling. All of these factors modify the dipole moment at the interface and the work function, which in turn impacts on charge transfer to an adsorbate. In addition, different types of imperfections at the interface may also affect the work function. For MgO/Ag a substantial 1.1-1.4 eV decrease in the work function has been measured and compared to the pristine Ag(100) surface^{61,62}. Calculations predict that the decreased values range from 1 to 1.4 eV depending on the applied functional^{52,63}.

Unlike line defects, the abundance of surface point defects such as oxygen vacancies in ultra-thin MgO films is very limited being about 0.1 %⁶⁴. Frequency-modulated dynamic force microscopy and STM have assigned these defects to regular F⁰ (two electrons) and singly occupied F⁺ (one electron) surface vacancies⁵⁴. Moreover, the concentration of oxygen vacancies can be artificially increased by bombarding the MgO films. Fabricated defects have been distinguished on the MgO surface employing variety of experimental techniques. While the electron paramagnetic resonance method⁶⁵ is sensitive only to F⁺ vacancies and electron energy loss^{66,67} and optical spectroscopies⁶⁸ can separate the vacancies only with support from computations, are F⁰ and F⁺ vacancies directly distinguishable in STM by their appearance in topographic images and different spectroscopic signatures^{65,69}. Despite the control reached over the stoichiometry at the surface of metal-supported ultra-thin films, it

is difficult to ensure that no vacancies are buried at the oxide-support metal interface as their experimental identification is challenging and therefore experimental studies on interfacial vacancies are sparse⁷⁰.

Well-ordered transition metal (TM) doped oxides such as CaO are prepared by adding transition metal atoms into Ca/O vapor grown as a tens of monolayers thick film on a metal support, where the topmost layers are synthesized without dopant atoms to prevent their segregation to the surface⁷¹. Mo doped CaO can also be formed by diffusion of Mo from the Mo substrate used for oxide growth. Figure 1 displays a typical structure setting used in computations. The presence of the dopant in the oxide matrix can be confirmed experimentally e.g., with Auger spectroscopy⁷¹. Formally TM ions adopt the oxidation state 2+ in MgO or CaO. In reality they can exist in various oxidation states, which can be easily changed. However, if a dopant adopts a different oxidation state, defect states must appear to maintain electroneutrality. The comparison of the impact of doping simple oxides with transition metal atoms Cr and Mo in MgO and CaO has been addressed by DFT calculations employing both PBE and hybrid functionals PBE0 and HSE06⁷². Calculations show that in Mo-doped CaO Mo favours a low-spin state with formal oxidation state 2+ and the impurity atom introduces a small 4% contraction to the metal-oxygen distance. Cr also adopts a 2+ oxidation state. In this case, the high spin state is thermodynamically preferred and lattice relaxations are small and mainly restricted to the nearest neighbour oxygen atoms owing to the similar radius of a host atom. The relative stability of different oxidation state-vacancy structures were analyzed with the help of atomistic thermodynamics at the PBE level. While Cr³⁺ in MgO-V_m (= one cation vacancy in the system) is the most stable structure under all reaction conditions, the oxidation state of Mo-CaO depends sensitively on the oxygen chemical potential ranging from Mo³⁺ to Mo⁵⁺ with decreasing chemical potential⁷².

III. ADSORPTION OF ATOMS, MOLECULES AND CLUSTERS ON ULTRA-THIN FILMS

A. Adsorption of individual Au atoms and clusters

Unlike bulk Au, nanosized Au exhibits high catalytic activity for various reactions⁷³⁻⁷⁶. In the pioneering work of Haruta and Hutchings, it was found that Au nanoparticles can

catalyze CO oxidation to CO₂ at low temperature^{75,77} and acetylene hydrochlorination^{75,78,79}. Later, Au nanoparticles were found to be active in reactions such as propylene epoxidation⁸⁰, hydrogenation of unsaturated hydrocarbons⁸¹ and nitrocompounds⁸², oxidation of diols⁸³ and alcohols⁸⁴, and the water-gas shift reaction⁸⁵. Different properties have been suggested to be important for catalytic activity of Au including size and structure of particles⁸⁶, low-coordinated step and corner sites⁸⁷, and the charge state of the active Au species^{88–91}. The catalytic activity of nano Au has been suggested to be sensitive with respect to the support material⁹². However, the recent discovery of high catalytic activity of Au clusters on a inert substrate indicates that the reducibility of a support is not a critical factor⁹³. DFT calculations suggest that MgO-supported Au particles are unable to activate a molecular oxygen, binding it weakly and having a high activation energy for dissociation⁹⁴. However, tiny Au clusters containing only few metal atoms on the same support display high catalytic activity towards CO oxidation^{88,95}. The perimeter sites at the Au-support interface have been suggested as active sites for CO oxidation on a TiO₂ support^{96–98}. At the interface, the low-coordinated sites in a Au particle have been found to be pivotal for O₂ activation^{99,100}. The studies on the adsorption of a Au adatom on a metal-supported MgO films highlight the difference in chemical characteristics of supported MgO films and bulk MgO surfaces.

On the basis of DFT calculations, it was predicted that Au atoms on MgO(100)/Mo(100) are negatively charged and their binding to the surface is stronger²⁸ than on a bulk-like MgO(100), where atoms stay neutral⁹⁴ and have adsorption energy of ~ -0.7 eV⁴⁸. On the supported thin film the adsorption site also changes: on the bulk MgO the Au atom is located on atop of an oxygen anion and on ultra-thin MgO a hollow/Mg site is preferred⁴⁸. The prediction of Au charging and the change in adsorption site were experimentally verified with STM measurements^{29,101}.

Calculations from Honkala and Häkkinen show that Au adsorption energy depends sensitively on film thickness being strongest on the thinnest film, Figure 2 with the exception that a 2ML-thick MgO film binds Au more strongly than a 1ML-thick film⁴⁸. In the case of 5 MgO layers on the Mo(100) surface, the Au adsorption energy on the O-top site is still twice as large as on the bulk-like MgO(100) surface. Figure 3 presents a density difference plot, projected on the plane that includes the Au adatom, displaying a rich polarization pattern for the 5ML-thick MgO film all the way from the MgO/Mo interface throughout the oxide. Additionally, substantial charge accumulation around Au is seen as well as charge

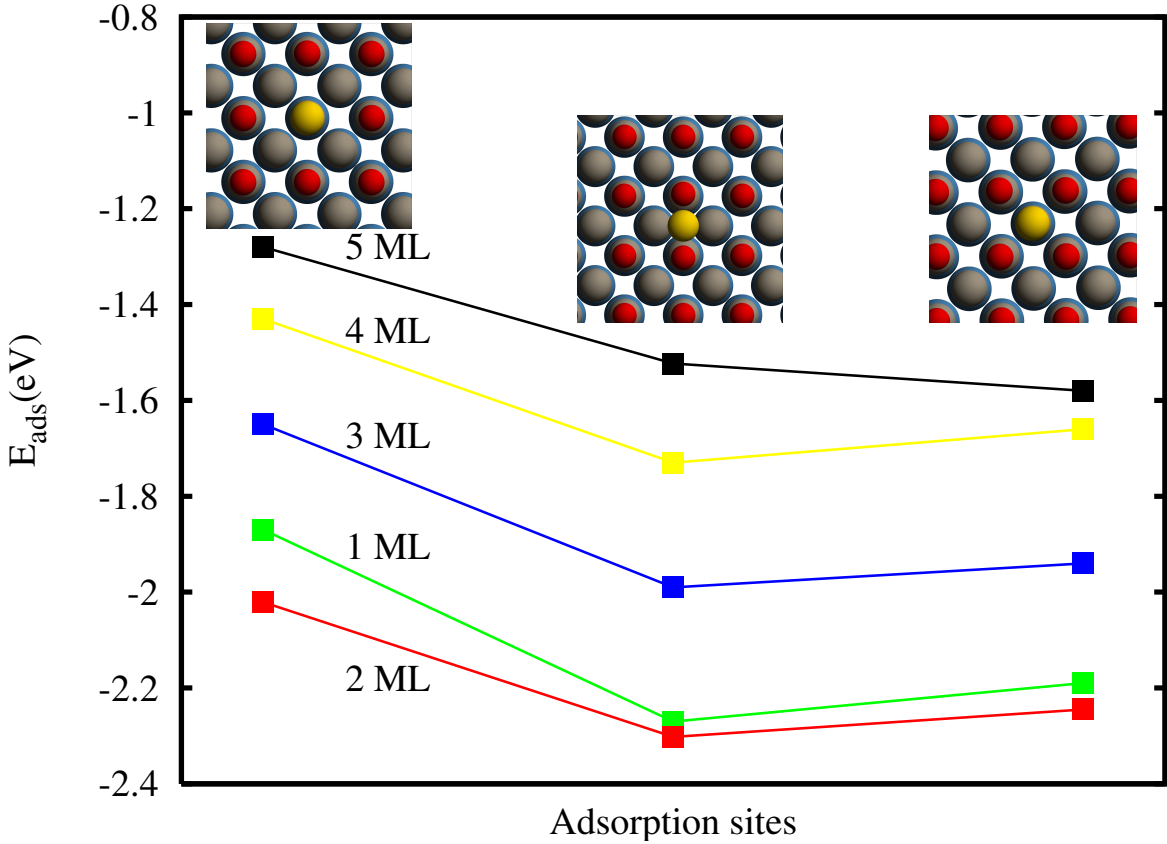


FIG. 2: Au adsorption energy at O-top, hollow and Mg-top sites on a Mo-supported MgO film with the film thickness ranging from 1 to 5 ML. Atomic color codes: yellow (Au), blue (Mo), red (O), and grey (Mg). Solid lines are just to guide the eye. Figure adapted with permission from Ref. ⁴⁸.

depletion at the surface.

On the 20ML-thick film, the most stable site is O-top and the difference in adsorption energy between single crystal and supported MgO systems is only about 0.2 eV, that is the supported film binds slightly more strongly¹⁰². If the Mo lattice constant is used for the single crystal MgO the difference reduces to 0.1 eV, which is within the limit of accuracy in DFT calculations. The Bader charge analysis^{103,104} shows that with increasing film thickness the Au charging decreases, which is in line with decreasing electron tunneling with increasing film thickness. This is also supported by the projected density of states as the Au 6s state moves toward the Fermi level with an increasing number of MgO layers and is singly occupied in the case of 20 layer system. On a bulk-like MgO surface the adsorption energy

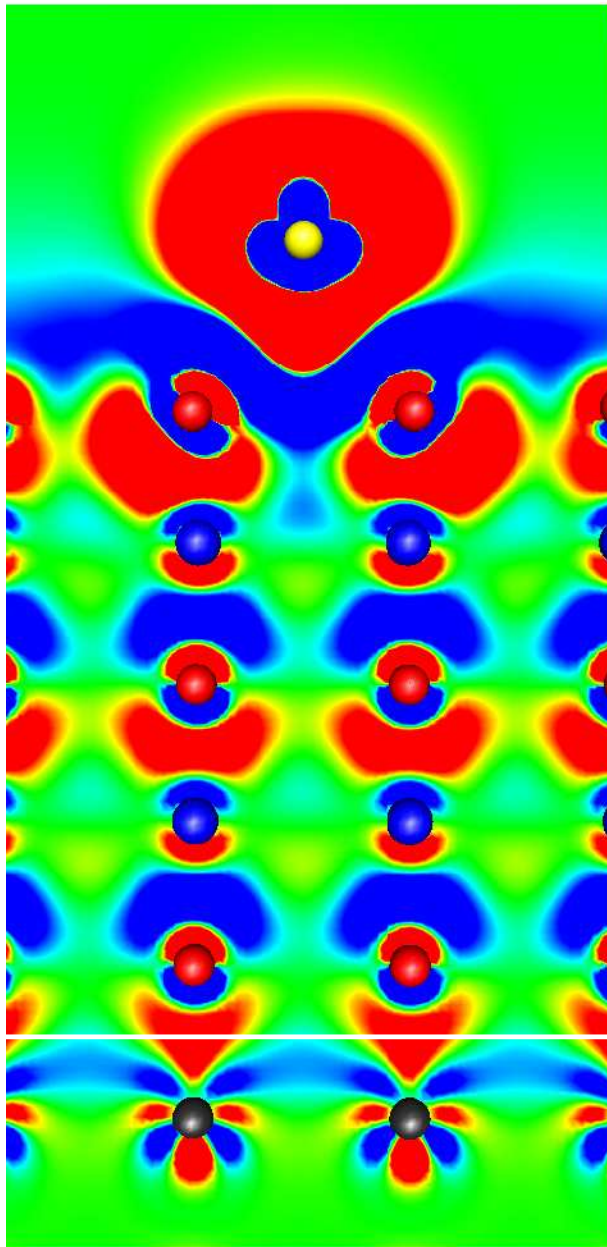


FIG. 3: Density difference plot for a Au atom at the hollow site on 5ML-thick MgO/Mo. Blue (red) regions indicate charge depletion (accumulation).

Yellow, red, blue, and black balls mark Au, O, Mg, and Mo atoms, respectively. The MgO-Mo interface is marked with the white line. The scale is (± 0.003 e/bohr³). Figure adapted with permissions from Ref.⁴⁸.

of metal atoms converges fast with film thickness¹⁰⁵. Calculations predict that the preferred adsorption site changes at the 10 ML- thick film of supported MgO¹⁰². This qualitatively agrees with experimental observations for Au/MgO/Ag, where the change in adsorption site takes place between three and eight MgO layers¹⁰¹.

Au charging introduces pronounced oxide relaxations, called polaronic distortion, around the adsorbate, which help to stabilize the state occupied by an extra electron. XPS experiments demonstrate the large deviation in the phonon structure of ultra-thin films and bulk oxides¹⁰⁶, which is associated to enhanced structural flexibility of the film being pivotal for structural relaxations to occur. In the case of Au on 2ML MgO/Ag, the Mg cation to which Au is bound to relaxes as much as 0.44 Å outwards according to calculations, and on the other hand the O anion below the cation relaxes 0.2 Å but toward the support metal³⁰. The energy contribution of this relaxation is substantial being ~ 0.7 eV for MgO(3ML)/Mo and ~ 0.95 eV for MgO(3ML)/Ag¹⁰². An unrelaxed substrate leads to weaker polarization, reduced charge transfer, and weaker adsorption. Thus, charging of Au is crucial to enhanced Au adsorption on the supported thin film. As the charge on the adsorbate originates from the metal-support interface, the work function of the combined metal-oxide system should be an important parameter. To understand how the work function variation affects adsorption energy of Au, the following systems were investigated: one Au atom on 2ML thick film on Mo, Pd, Pt, Ag, Au surfaces¹⁰². In these calculations the equilibrium lattice constant was employed for each metal, introducing unequal strain to the supported MgO film that can potentially impact on the obtained results. Figure 4a) shows calculated work functions for the clean (100) metal surfaces and for metal-supported 2ML thick MgO films. For the studied metals the work function ranges from 4.1 eV (Mo) to 5.6 eV (Pt). The presence of MgO film reduces the work function by ~ 2 eV owing to polarization at the interface. Figure 4b) displays the variation of Au adsorption energy. In general, the tendency is that the low work function is associated to more exothermic adsorption energy but the values are scattered. The adsorption energies range from ~ -2.1 eV on a Mo-supported MgO film to ~ -0.6 eV on Pd-supported MgO film. This highlights the fact that the selection of a support metal is an adjustable parameter that can modify the binding strength of an Au atom in addition to the thickness of the film. Interestingly, the Bader charge analysis shows that the amount of charge transferred to Au is almost independent of the supporting metal and the work function¹⁰².

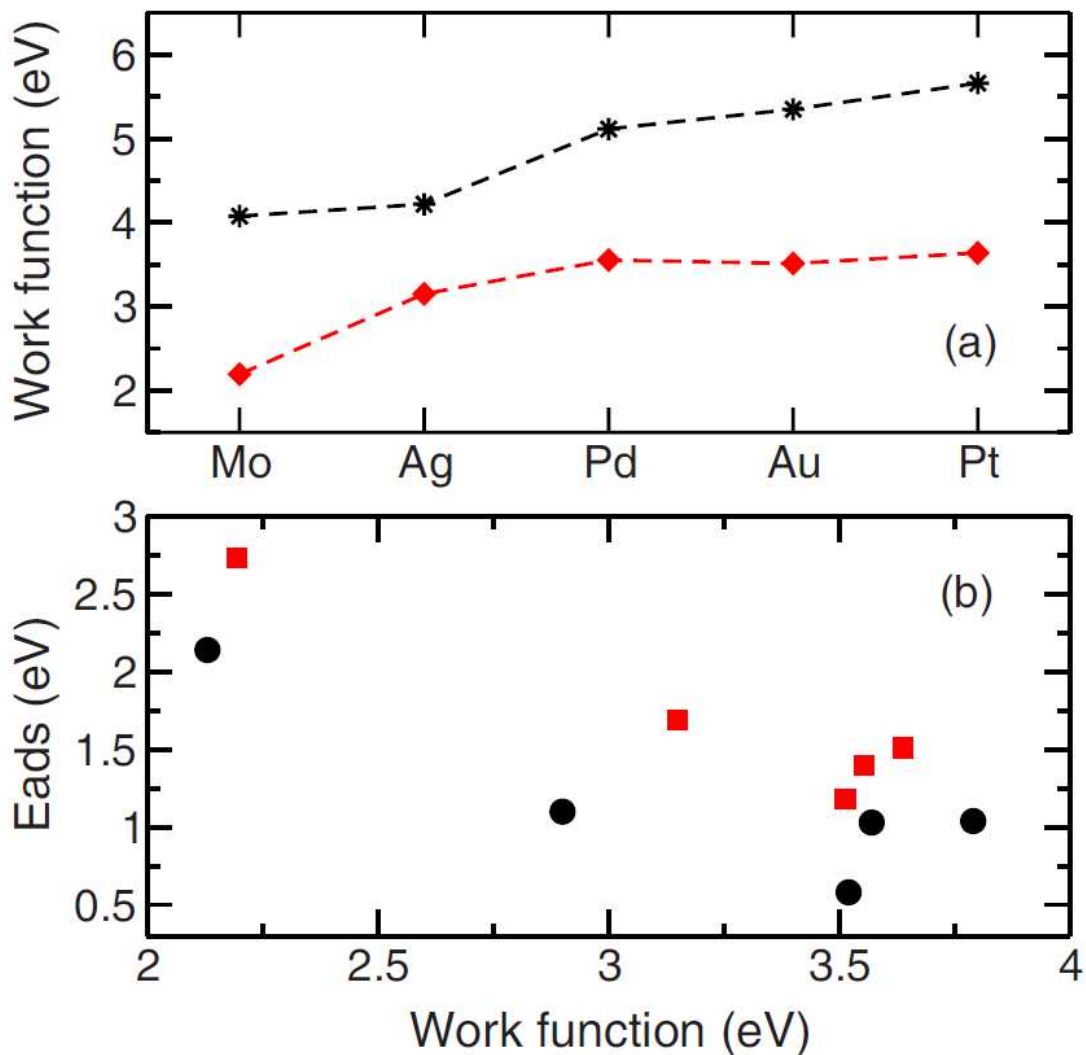


FIG. 4: (a) Calculated work functions for Mo, Ag, Pd, Au and Pt surfaces (stars) and corresponding values for metal-supported MgO(2ML) systems (diamonds). (b) Adsorption energies for Au (circles) and NO₂ (squares) as a function of work function. Note, that here positive adsorption energy values stand for exothermic adsorption. Figure adapted with permission from Ref.¹⁰².

The large modifications in adsorption owing to the metal support are not limited to Au or other transition metal single atoms, but significant changes are also seen in Au cluster geometries, charge states, and adsorption energies on metal-supported MgO films¹⁰⁷⁻¹¹¹. For comparison, on bulk MgO the smallest Au_N (N=2-6) clusters favour minimal wetting with

one or two Au atoms in contact with oxide ions^{28,94,108,112,113}. The internal atomic structure follows the calculated structures of corresponding neutral gas-phase species¹¹⁴. The binding is rather weak with adsorption energies ranging from -0.6 eV to -1.4 eV showing no clear size dependence¹⁰⁸. The nature of the weak Au-MgO interaction has been characterised to be of polarization type¹¹⁵.

From an interplay between STM experiments and DFT calculations it was shown that in the size regime of 2-6 atoms, the most stable Au clusters are linear chains on an Ag supported MgO film¹⁰⁹. The smallest Au aggregates also adopt linear structures on MgO/Mo substrates¹¹¹ as shown in Figure 5. For Au₁₋₃ only chain isomers are stable and their adsorption energies vary from -1.3 eV to -2.8 eV on MgO/Mo(100). The adsorption energies of planar Au₄₋₆ range from -1.1 eV to -2.1 eV¹⁰⁸ while the chain structures of the same size bind 1.2-1.5.eV stronger¹¹¹. The Bader charge analysis shows that the charge state of the adsorbed cluster depends on the atomic structure and impacts on adsorption energy. The linear Au₁₋₃ and planar Au₄₋₆ aggregates are singly charged whereas the Au₄₋₆ chains are doubly charged. The singly charged isomers are structurally similar to their anionic gas-phase counterparts^{43,108} while linear cluster shapes do not have counterpart in the gas-phase or on a single crystal MgO surface. Charging behaviour of Au₂₋₆ chains on supported MgO films is independent of the support metal either Mo or Ag¹⁰⁹. On Al₂O₃/NiAl, the charging effect is larger as Au₃ contains already two and Au₅₋₆ three extra electrons¹¹⁷. The electronic states of Au chains can be analyzed by means of one dimensional quantum well state model. In such a model, the electronic structure of the aggregates is determined by a potential well to which 6s¹ valence electrons of individual Au atoms are delocalized and confined. Au chains on Al₂O₃(2ML)/NiAl(110) display a particle in a box-type of behaviour as shown by experiments and calculations¹¹⁷. Figure 6 exhibits similar behaviour for Au chains on MgO(3ML/Mo), where HOMO and LUMO states of Au₃ and Au₆ chains are shown together with the 1D harmonic oscillator potential and the probability density of corresponding eigenstates. The LUMO state of Au₃ has three lobes and two nodes and the HOMO orbital has two lobes and one node. These equal to the HOMO and LUMO states of the 1D harmonic oscillator with 4 electrons, each Au 6s orbital donates one electron while the fourth electron comes from the substrate. This is in line with Bader charge of -1.03 for the adsorbed chain. In the case of Au₆, the LUMO state has 5 lobes and 4 nodes whereas the HOMO state has 4 lobes and 3 nodes. This stands for the 1D harmonic oscillator with

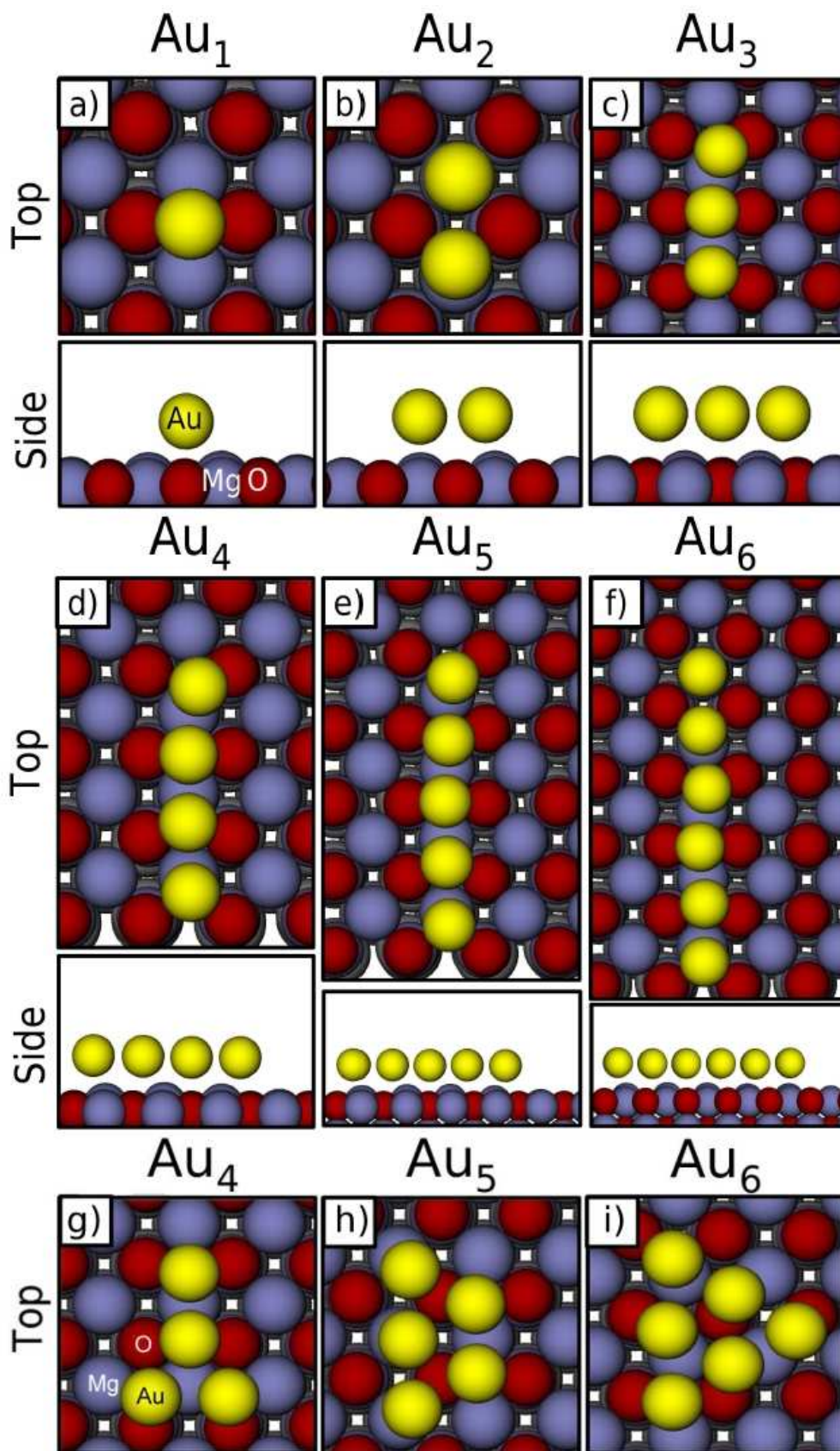


FIG. 5: The top and side view of the most stable Au₁₋₆ adsorption geometries on MgO-supported Mo are given in a-f, and the top view of less stable 2D planar structures for Au₄, Au₅, and Au₆ are presented in g-i. Au atoms are yellow and Mg and O atoms are blue and red, respectively. Mo atoms are not shown. Figure adapted with permission from Ref.¹¹⁶.

eight electrons. Six out of eight electrons originates from Au atoms while the other two electrons are from the substrate. Again, this agrees nicely with the calculated Bader charge, which is $-2.39 e$ for Au_6 ¹¹¹.

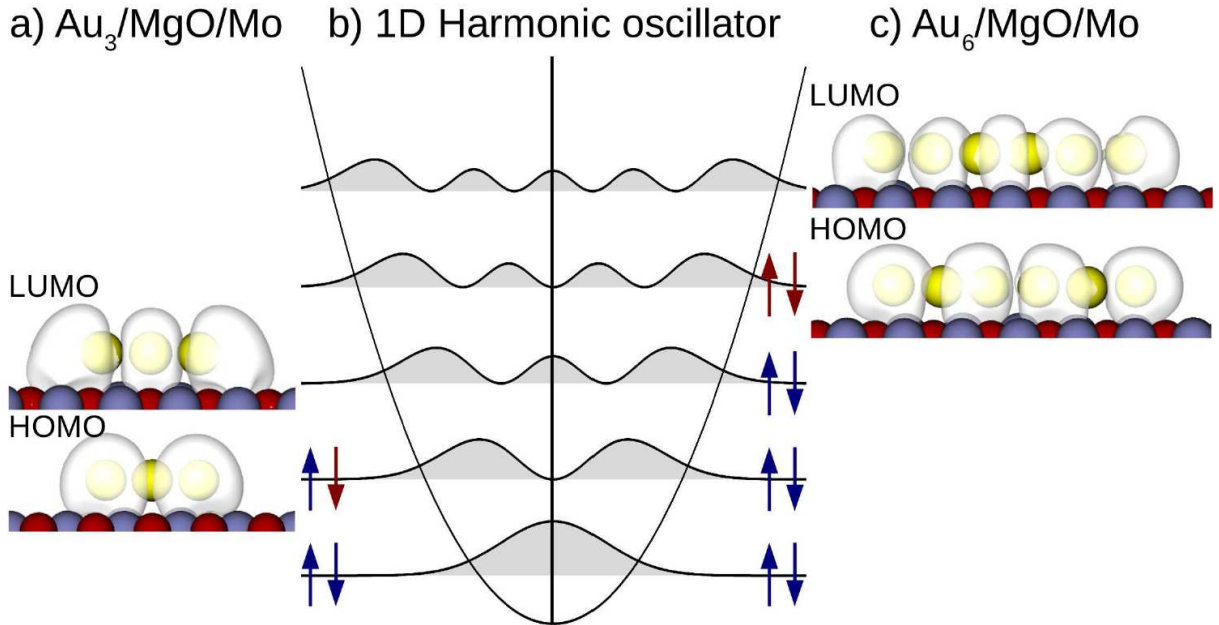


FIG. 6: The spatial appearance of the HOMO and LUMO states of Au_3 panel a and Au_6 panel c on $\text{MgO}(3\text{ML})/\text{Mo}$ together with their connection to a 1D quantum well model panel b. The blue arrows stand for the valence electrons from the atomic Au 6s states and the red arrows correspond the electrons transferred from the substrate. Figure adapted with permission from Ref.¹¹⁶.

The tendency of Au clusters to prefer 2D structures over 3D structures was first predicted by DFT calculations for Au_n ($n=8,16,20$) on Mo-supported MgO ¹⁰⁷ and later verified experimentally with STM on an Ag-supported MgO film as a function of the film thickness¹⁰¹. The strong interaction with the surface introduces reoptimization and straining in the internal cluster geometry. Calculations show the favourably of planar structures compared to 3D ones on the 2 ML thick film, but with increasing film thickness Au adhesion to the substrate weakens leading eventually to the preference of 3D structures¹⁰⁷. STM experiments demonstrate that the cluster geometry is sensitive to the film thickness, and 3D clusters are seen on the 8 ML-thick film whereas 2D clusters are present on the 3 ML thick film¹⁰¹. DFT calculations

predicted charge transfer to be present also on larger clusters^{107,118}. While the direct experimental verification of charge transfer is challenging the 2D shape of the adsorbed cluster has been taken as an indirect indication of a charge transfer process. To further explore the internal electronic structure and charger transfer of small MgO/Ag-supported Au clusters, a combined STM-DFT study was undertaken¹¹⁹. Similar to Au chains, larger Au clusters prefer to maximize their contact area with the support and become negatively charged with the calculated average charge transfer of $-0.2 e^-$ an Au atom. Charged Au aggregates need to reduce substantial electron-electron repulsion originating from excess charges. This can be achieved by separating extra electrons over long distances, which results, for example, in the localization of electrons at the edges of the islands and leads to a further stabilization effect of linear and planar structures¹²⁰.

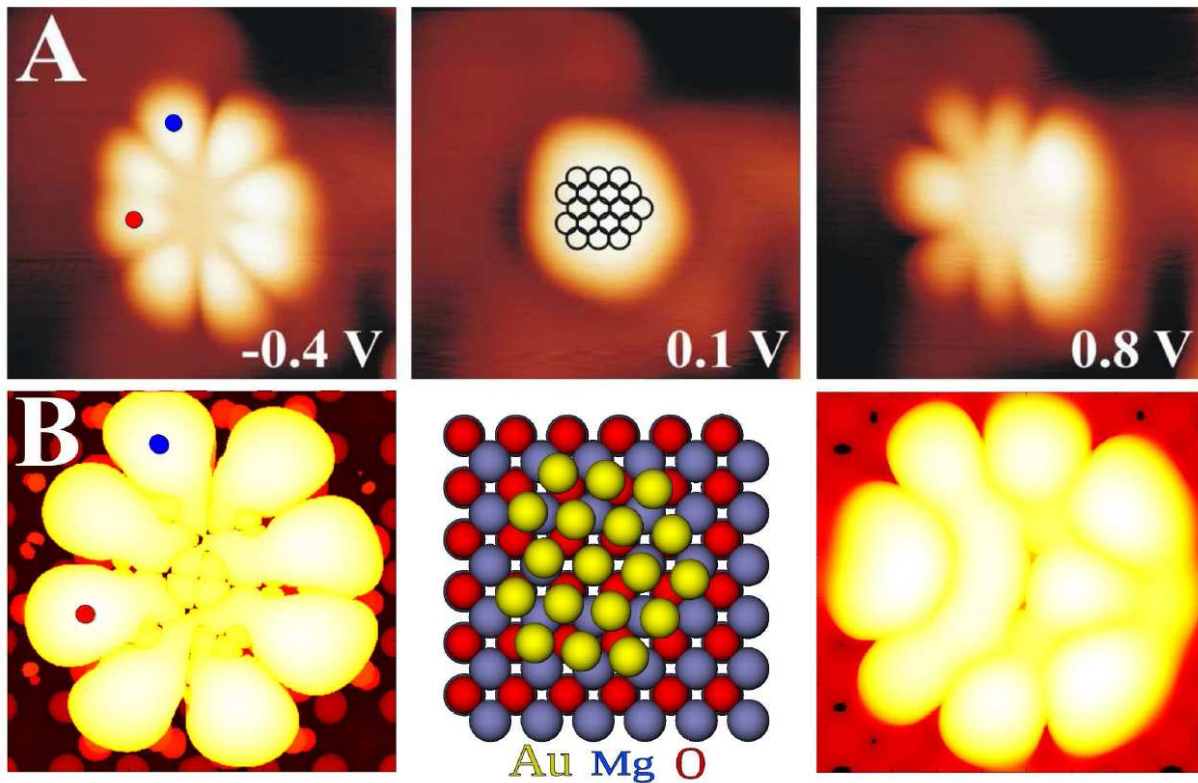


FIG. 7: Panel A) Measured STM images of a selected Au cluster on Ag-supported MgO at bias voltage -0.4 V (HOMO), -0.1 V, and $+0.8$ V (LUMO). Panel B) The calculated STM images of HOMO and LUMO states $\text{Au}_{18}/\text{MgO}(2\text{ML})/\text{Ag}$. The atomic structure of the calculated system is shown in the middle. Figure adapted with permission from Ref.¹¹⁹.

Figure 7 A) displays measured constant-current-mode topographic STM images of a selected Au cluster on an Ag-supported 2ML-thick MgO film. At low bias a featureless bright image appears because tunneling is not in resonance with any cluster states. Adjusting the bias to appropriate values, flower-like shapes appear and the increase in cluster height is seen. Both effects suggest that the STM contrast is dictated by electronic structure of a cluster whose exact atomic structure remains unknown. Theoretically, the electronic structure of a planar cluster can be predicted employing the 2D harmonic oscillator potential model, which confines the atomic 6s valence electrons¹¹⁸. The eigenstates of the 2D harmonic oscillator (HO) can be characterised by their principal quantum number together with the projection of angular momentum on the normal vector of the plane, m . Thus, the states have $n-1$ radial nodes and $|m|$ angular nodes. The atomic nomenclature of the states is adopted, which means that e.g., the 2P state has one radial node and two angular nodes. Moreover, states such as 1F exhibit a very flower-like appearance. Again, each Au atom brings in one 6s electron, therefore the number of atoms in a cluster can be obtained by analyzing the nodal structure of frontier orbitals in a cluster within the 2D HO model.

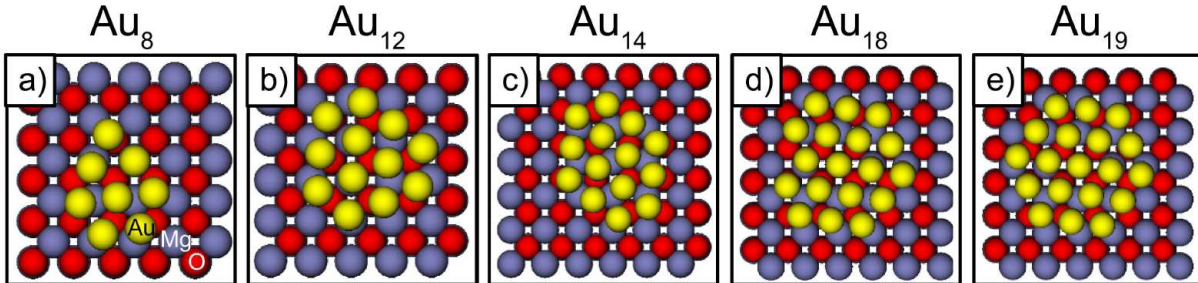


FIG. 8: Selected highly symmetric candidate structures for Au_{8-20} clusters addressed by DFT calculations. Figure adapted with permission from Ref.¹¹⁶.

To resolve the atomic structure of these clusters, an extensive DFT search for possible structures was carried out at size regime of 6-20 Au atoms per a cluster. The aim was to find clusters having similar HOMO and LUMO states as seen in STM images of unknown species. The candidate cluster sizes were selected so that the 2D HO model predicts that their HOMO and LUMO states resemble those seen in experiments. Furthermore, since flower-like shapes are typical for symmetric planar clusters the computational search focused on these structures. Similar to 1D Au chains Au clusters might have additional electrons not originating from 6s states. Figure 8 collects some of the selected cluster sizes and shapes

calculated. All of them experience thin-film effects that is having a planar geometry with formation energies ranging from -2.1 - -2.5 eV/atom. The charge analysis suggests that the smallest species are doubly charged, and the large ones can accommodate 3-4 electrons. Calculations assign that Au₁₈ contains altogether 21.5 electrons: 18 from 6s states and 3.5 from the support. Within the 2D HO model it was not possible to unambiguously distinguish the charge state. However, comparison of calculated HOMO and LUMO states of Au₁₈ shown in Figure 7B match perfectly with the HOMO and LUMO states of unknown species in Figure 7A. The final confirmation was obtained by comparing the measured and calculated dI/dV spectra from the same spot on the cluster showing the same sequence of states and intensity modulation¹¹⁹. Calculations show that simulated STM images are highly sensitive to the number and arrangement of Au atoms in the cluster¹¹⁶ and therefore the unknown cluster was identified as Au₁₈ and not to Au₂₀⁻², which according to the charge analysis should not even exist as adsorbed Au₂₀ gains 4 electrons. The electronic structure of larger, ultra-thin film-supported, clusters containing 50-200 atoms has been analyzed combining STM measurements, a theoretical particle-in-a-box model, and tight-binding DFT calculations showing again a nice agreement between measurements and calculations¹²¹. Finally, the charge transfer does not always occur from the metal-oxide interface towards the adsorbed Au as reported for the FeO/Pt(111) surface, where Au atoms form positive ions¹²². The formation of Au anions on metal supported MgO films and cations on FeO/Pt(111) highlight the influence of the work function on the charge transfer in ultra-thin film systems. While MgO reduces the work function of both Mo and Ag and thus facilitates electron transfer to the 6s orbital of an Au atom, quite opposite happens in the case of the FeO/Pt(111) system, which has very high work function and the 6s state is pushed above the Fermi level and electron transfers to the surface¹²².

B. Adsorption of other atoms than Au

Despite Au adsorption on metal-supported ultra-thin MgO films have received majority of interest, the adsorption of other atoms such as K, Pd, Pt, Ni, Cu, and Ag have been addressed with DFT computations^{28,58,123}. Coinage metals Cu and Ag exhibit completely different adsorption behaviour on MgO and MgO(2ML)/Mo(100) surfaces: on a bulk oxide surface they favour O anions, while on a metal-supported thin film all adsorption sites (hollow,

cation and anion) are almost equally favoured. The presence of Mo enhances the adsorption energies by 0.5 eV and 0.8 eV for Cu and Ag atoms, respectively¹²³. The analysis of charge states shows that on bare MgO both species are neutral but become negatively charged on the supported film. Changing the support metal to Ag introduces marked differences compared to Mo: adsorption energies are close to values on bare MgO and no charge transfer is observed meaning that atoms stay neutral.

At variance with coinage metals, group 10 atoms interact strongly with the bare MgO. They have adsorption energies varying from -1.44 eV (Pd) to -2.56 eV (Pt), which favour adsorption on anions and display strong corrugation of the potential energy surface¹²³. The Bader charge analysis shows nonzero values owing to the mixing of metal and oxide states. However, it does not indicate charge transfer but merely demonstrates the formation of a covalent polar bond. On MgO(2ML)/Mo(100), the adsorption of both Pd and Ni atoms is enhanced (~ 0.4 eV) and the Bader, density of states, and magnetic moment analysis suggest the existence of a small charge transfer; yet neither of species cannot be classified as a full anion because of the substantial mixing with the O 2p states and the covalent nature of the bond. Pt becomes a full anion on MgO/Mo(100) with adsorption energy of ~ -3.3 eV on a O-top site, and considerable, 0.3 \AA , relaxation of the lattice O underneath. The adsorption characteristics of all three group 10 atoms on MgO(2ML)/Ag(100) are very similar to those on the bare support highlighting the fact that the nature of atoms can be tailored by varying the substrate. The reason for all of these transition metal atoms being neutral on MgO(2ML)/Ag(100) is the higher work function ~ 3 eV compared to MgO(2ML)/Mo(100) for which the cost to remove an electron is ~ 2 eV.

Finally, the adsorption of a K atom on MgO(2ML)/Ag(100) is briefly discussed⁵⁸. The presence of Ag support stabilizes K adsorption by ~ 0.3 eV on the most stable O-top position, and large lattice relaxations are seen. Yet, adsorption is very weak being less than -0.5 eV. Interestingly, the K atom becomes positively charged donating charge to the Ag support. Positive charging is further supported by decrease in a K-O distance by 0.33 \AA and decrease in the work function of K/MgO(2ML)/Ag(100) system compared to MgO(2ML)/Ag(100).

C. Adsorption of NO₂ and O₂ molecules

Enhanced adsorption on metal-supported ultra-thin film is not limited to metal species. The phenomenon is more general in nature and present also for molecules with high electronic affinity such as O₂ and NO₂. Understanding NO₂ adsorption characteristics is important, for example for NO_x storage catalysts to control emissions from combustion in oxygen excess¹²⁴. On bulk-like MgO NO₂ adsorbs weakly and stays neutral¹²⁵, whereas DFT calculations render NO₂ adsorption strongly enhanced on metal supported MgO¹²⁶. The molecule becomes negatively charged forming a NO₂⁻¹ anion, which is also singled out by strong structural changes in a N-O bond length and a O-N-O angle¹²⁷. Figure 9 displays the most favourable NO₂ adsorption geometry on a MgO(2ML)/Pt(100) surface. Similar adsorption characteristics are seen on a more complex Al₂O₃ film supported over Ag, where according to calculations NO₂ adsorption energy is enhanced by factor of 5¹³. This takes place with concomitant substantial structural relaxations at the metal-oxide interface, where in particular, the Ag-O distance is strongly reduced. Among the studied metal supported ultra-thin oxides, BaO/Pt(100) shows the largest stabilization effect and NO₂ adsorption energy is about -2.4 eV on the 2ML thick film¹²⁸. On 2ML Al₂O₃ (0001)/Ag and MgO/Ag(100) films the corresponding adsorption energies are -2.0 eV and -1.8 eV, respectively¹⁰².

The extent of structural relaxations depends on oxide and support metal but also on an adsorbate being more pronounced for NO₂ than for Au even though both species are singly negatively charged¹⁰². The binding strength of NO₂ as a function of increasing film thickness resembles that of Au, since it becomes weaker with increasing film thickness. The unusual feature of the Al₂O₃/Ag system is that the calculated work function is larger than that of the bare metal, which is in contrast what is found for metal-supported MgO¹⁰². The increase results from the different interface structure: while in the case of MgO the metal atoms are below anions, they are under cations in the Al₂O₃(0001)/Ag(111) system leading to polarization towards oxide and increase in the work function¹⁰². The charging of species on metal supported ultra-thin films has been linked to the reduced work function⁵⁸ but the Al₂O₃/Ag system shows that this is not necessarily the case.

Calculations predict that the stabilization, charging and internal structural modifications of O₂ adsorbed on metal supported MgO resemble that of NO₂ and highlight the spontaneous formation of an activated superoxo species^{20,111} owing to the low work function of the system.

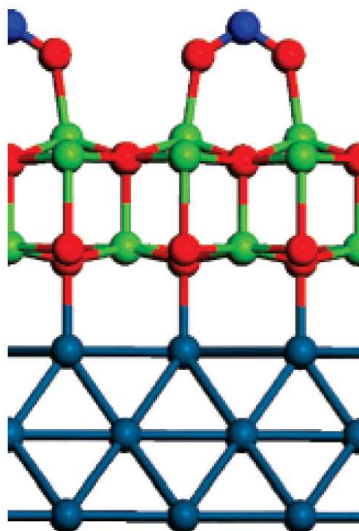


FIG. 9: The most favourable adsorption geometry of NO_2 on Pt-supported MgO ¹²⁷.

Mo atoms are coloured dark blue, oxygen atoms red, magnesium atoms green, and the bright blue atom stand for a nitrogen atom. Reprinted with permission from *Journal of Physical Chemistry B*. Copyright 2006 American Chemical Society.

While on a single crystal $\text{MgO}(100)$ surface O_2 adsorption is endothermic and the molecule stays neutral, on a metal supported $\text{MgO}(100)$ film O_2 adsorption is exothermic, the molecule becomes singly charged, and the O-O bond length increases^{20,111}. O_2 adopts a parallel adsorption geometry bridging between two Mg cations with adsorption energy of -0.82 eV on an Ag-supported film²⁰. On Mo-supported MgO the adsorption energy is even more exothermic being -1.5 eV¹¹¹. The theoretical prediction of O_2^- formation was confirmed by means of EPR spectroscopy¹²⁹, where an unpaired electron is responsible for the signal. The common feature of the species that show enhanced adsorption on metal-supported ultra-thin films is that they have high enough electronic affinity. Molecules with lower electron affinity such as CO do not show increased stability²⁰.

IV. CHEMICAL REACTIONS OF SIMPLE MOLECULES ON ULTRA-THIN FILMS AND SUPPORTED AU CLUSTERS

Relatively little attention has been paid on chemical reactions on MgO due to its inertness compared to more reactive reducible oxides such as TiO₂. However, as discussed above ultra-thin films display higher chemical reactivity compared to bulk MgO binding species with high electron affinity more strongly. The question then arises: can thin films systems facilitate chemical reactions ?

A. CO oxidation on ultra-thin films

Recent DFT calculations of Hellman *et al.* predict that CO oxidation proceeds over an Ag-supported ultra-thin MgO(100) film with an activation barrier lower than the corresponding barrier on Pt(111)²⁰. While CO oxidation on Pt involves O₂ dissociation before CO oxidation¹³⁰, on MgO/Ag O₂ dissociation is highly unfavourable being endothermic by 1 eV. Also CO adsorption is weak being only -0.25 eV on bare MgO/Ag and -0.4 eV on the oxygen preadsorbed surface. The calculations give an activation barrier of 0.7 eV if both reactants are adsorbed to the surface prior the reaction but the barrier drops to only 0.3 eV for the Eley-Rideal route, where gas-phase CO reacts directly with the adsorbed molecular oxygen.

For comparison, on FeO/Pt(111) a completely different reaction mechanism has been put forward¹⁵ owing to the high work function of Pt, which prevents the spontaneous formation of O₂⁻¹ anions. Calculations predict that O₂ dissociation is a relatively easy process, where the adsorption energy of O₂ is -0.7 eV and the dissociation is strongly exothermic with a modest activation barrier of 0.4 eV. At high O₂ coverage this leads to the transformation of a bilayer film to trilayer FeO_{2-x} stoichiometry as seen in Auger electron spectroscopy and temperature programmed desorption¹⁵. A similar transformation is seen when NO is used as an oxidative agent²¹. On FeO₂/Pt(111) CO oxidation involves the extraction of lattice oxygen and the barrier for CO₂ formation is only 0.2 eV according to DFT calculations¹⁵. At the end, oxygen vacancies are healed via a reaction with a gas-phase oxygen, which returns the original stoichiometry of the film. A combination of various experimental techniques show that O-rich FeO_{2-x} films produced by O₂ and NO are virtually identical, the substantial

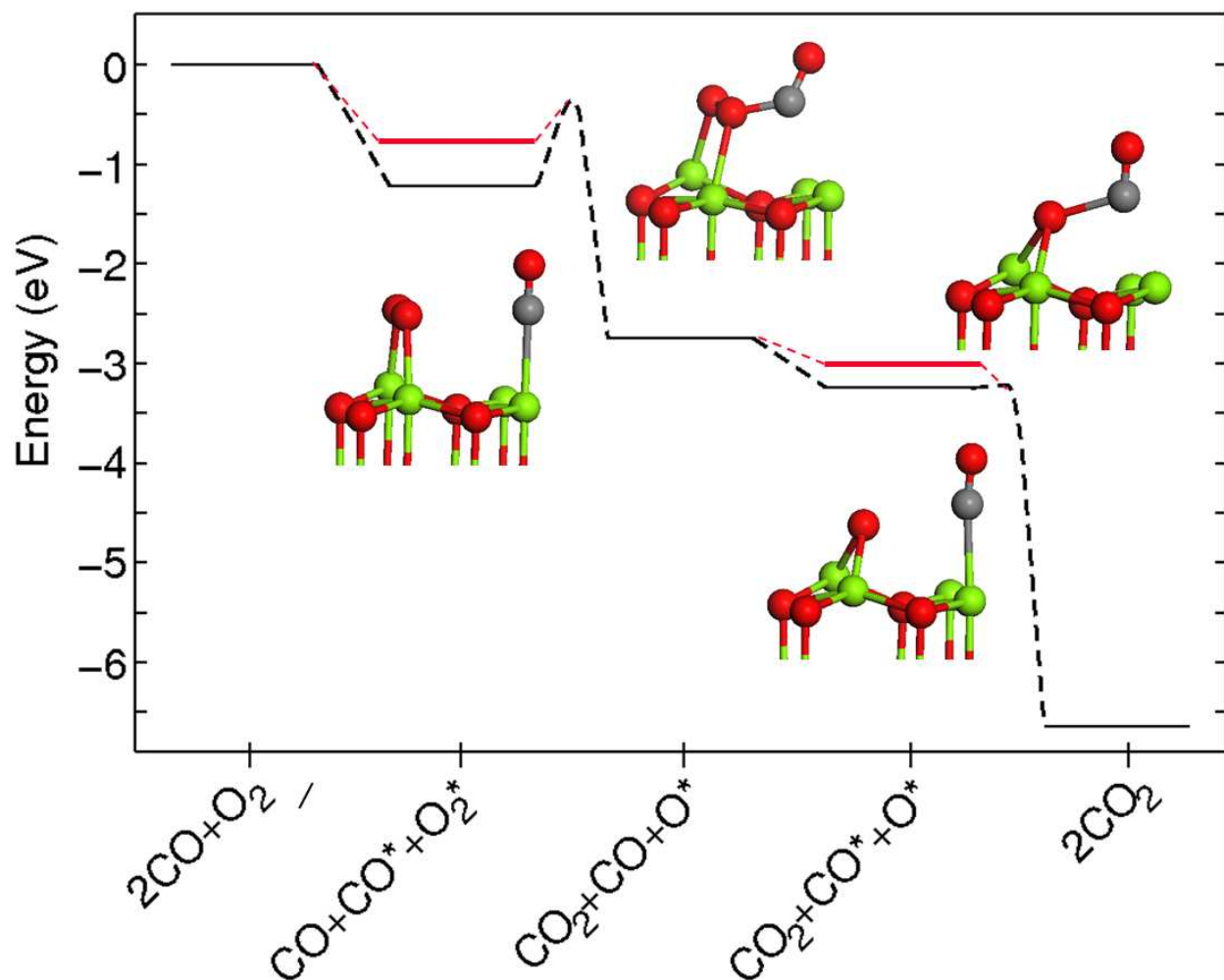


FIG. 10: The potential energy surface for CO oxidation over MgO(100)/Ag(100)²⁰. The black line corresponds the Langmuir-Hinshelwood reaction mechanism. The energies related to the Eley-Rideal mechanism are marked with the red bars in reaction steps, where Eley-Rideal and Langmuir-Hinshelwood energies differ. Atomic color codes: green (Mg), red (O), and gray (C). Reprinted with permission from Journal of American Chemical Society. Copyright 2009 American Chemical Society.

difference in kinetics of CO_2 production from $\text{CO} + \text{O}_2$ and $\text{CO} + \text{NO}$ reactions indicate that the healing of oxygen vacancies is the rate-limiting step²¹. DFT calculations demonstrate that this is indeed the case because NO adsorbs N-down on an oxygen vacancy and CO reaction with the "dangling" oxygen is a highly activated process²¹.

B. Adsorption and reactivity of O₂ and CO on Au clusters supported by ultra-thin films

The adsorption and activation of O₂ is known to be difficult on Au¹³¹, yet its pivotal role in oxidation reactions on an Au catalyst is undeniable. Therefore, it is natural that first reactivity studies on ultra-thin film supported Au clusters include molecular oxygen. O₂ adsorption and activation on thin-film supported Au clusters has been theoretically analyzed on Au₁₋₆/MgO/Mo¹¹¹ (Figure 11), on Au₁₄ and Au₁₈ /MgO/Ag¹⁹, and on Au₂₀/MgO/Mo¹³². Calculations show that molecular oxygen slightly favours adsorption on the bare MgO/Mo surface than on Au₁₋₆/MgO/Mo¹¹¹. While O₂ adsorption on the supported Au₂₋₆ chains is exothermic with adsorption energies ranging from -1.5 eV to -0.7 eV and weakest adsorption found for Au₄, no stable adsorption geometry could be found on a single Au atom. In general, O₂ prefers to adsorb to the end of the Au₂₋₆ chains bridging simultaneously two Mg cations, similarly to the bare MgO/Mo. Upon adsorption, O₂ gains approximately one electron, O-O bond length elongates to 1.39 - 1.47 Å depending the cluster size, and the O-O bond length correlates linearly to the calculated charge state of the molecule as depicted in Figure 12¹¹¹.

Figure 13 shows that O₂ adsorption on MgO/M-supported Au chains is more exothermic than adsorption on neutral, anionic, and dianionic gas-phase clusters. The clear oscillatory adsorption trend with respect to a number of Au atoms in the chain, that is typical for gas-phase or F_s/MgO adsorbed clusters, is absent. Adsorption and dissociation of multiple O₂ molecules was calculated at the edges of a flat Au₁₄ cluster supported by MgO(2ML)/Ag¹⁹ and is strongly linked to bridge the materials and pressure gaps to discover potential morphology changes of the catalyst particle under ambient conditions. The Au₁₄ cluster has an idealized C_{2v} symmetry with ten atoms at the edge and four inner atoms forming a rhombus-like structure. All the favourable adsorption sites reside at the edge of the cluster as the adsorption on the top of the cluster is endothermic. For all the studied structures adsorption energies range from from -1.15 eV for a single molecule to -0.6 eV for the 10'th molecule. The best adsorption structures for 1, 2, 6, and 10 oxygen molecules are given in Figure 14. Depending on the number of oxygen molecules two adsorption modes are identified: perpendicular and parallel, where either one or two oxygen atoms interact with Au edge atoms. Electronic and geometric adsorption characteristics group into two categories

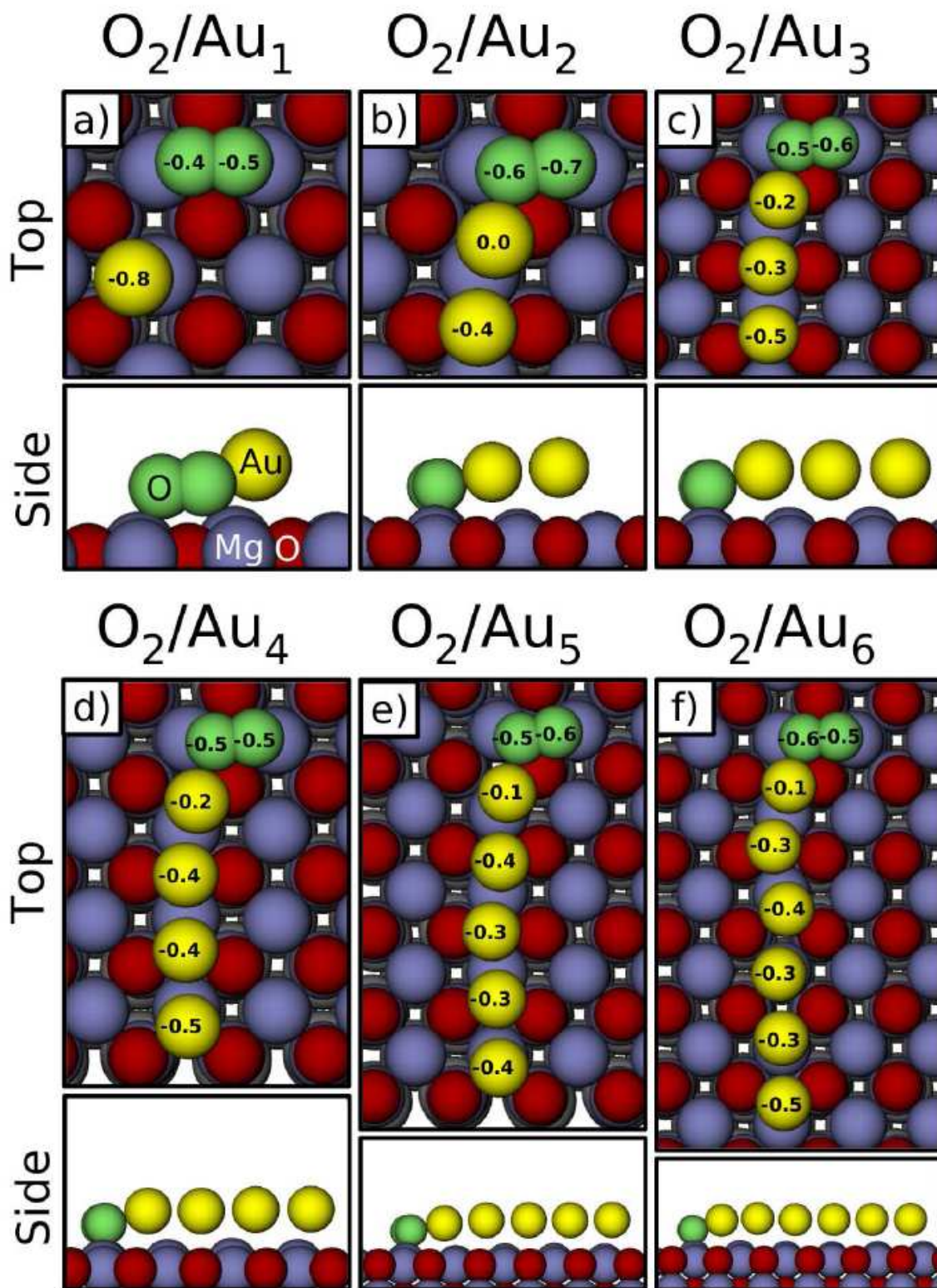


FIG. 11: The top and side views of the optimal geometries for molecular oxygen on Au_{1-6} aggregates on $MgO(3ML)/Mo$. the colour coding is as follows O_2 green, Au yellow, Mg blue and lattice O red. The Bader charges of selected atoms are marked in the atoms. Figure adapted with permissions from Ref.¹¹¹.

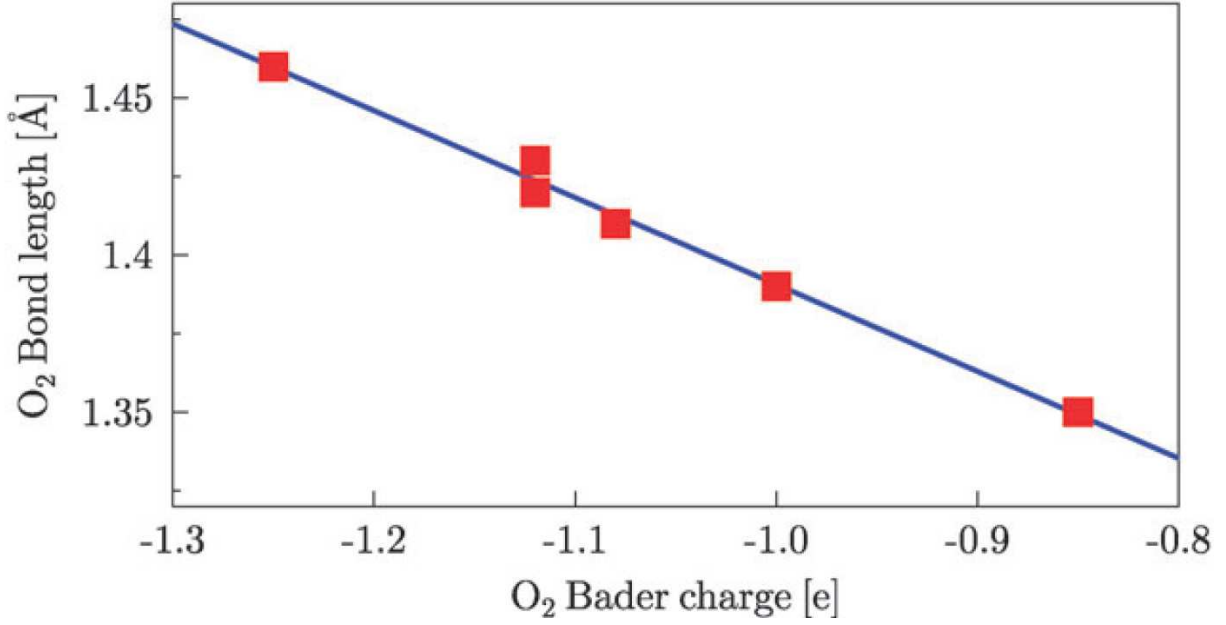


FIG. 12: The O_2 bond length as a function of the O_2 Bader charge for $O_2/Au_{1-6}/MgO/Mo$. Figure adapted with permissions from Ref.¹¹¹.

mode	O-O (Å)	Bader (e)	μ_B
parallel	1.44-1.53	-1.0 - -1.3	0
perpendicular	1.31-1.37	-0.7	1

TABLE I: The calculated O-O bond length in Å , a calculated Bader charge, and magnetic moment for an O_2 molecule adsorbed either on the parallel or perpendicular fashion at the perimeter of the Au_{14} cluster over $MgO(2ML)/Ag(100)$ ¹⁹.

relative to the orientation as shown in Table I.

All the analyses support an interpretation that in the perpendicular mode the electronic state of O_2 resembles superoxo, while the parallel mode corresponds to the peroxo-like species. At low coverage O_2 favours parallel adsorption mode at the perimeter of cluster. With increasing O_2 coverage, the perpendicular mode becomes dominating and it is the only possibility to accommodate 10 molecules to the perimeter of Au_{14} . Interestingly, the differential adsorption energy of tenth O_2 is still considerable being -0.75 eV exothermic and highlights the ability of MgO/Ag -supported Au_{14} to bind and activate simultaneously

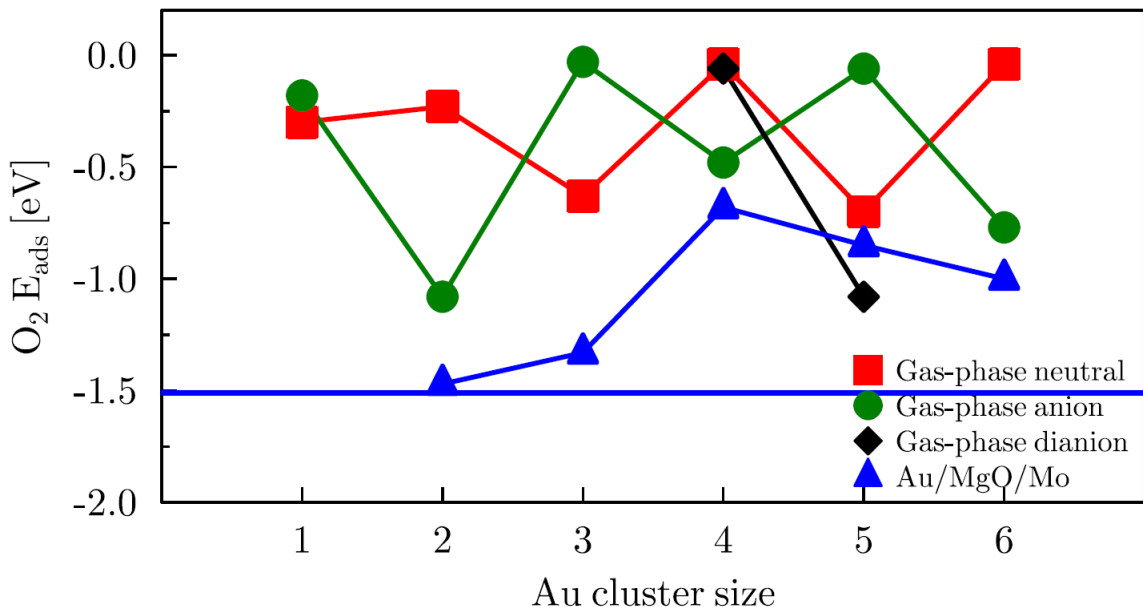


FIG. 13: The adsorption energy of molecular O_2 on chain-like clusters on $MgO(3ML)/Mo$ (blue triangles) as well as on selected neutral (red squares)¹³³, anionic (green circles)¹³³, and dianionic (black diamonds) gas-phase clusters. The horizontal blue line gives the adsorption energy on the bare substrate. Figure adapted with permissions from Ref. ¹¹¹.

multiple oxygen molecules. This theoretical prediction is yet to be experimentally verified on thin film supported Au cluster. While for a MgO/Mo supported Au cluster this might be impossible as O_2 prefers to adsorb on a bare film to the cluster, from the thermodynamic aspect experimental verification should be possible for the $MgO/Ag(100)$ support, where the O_2 species clearly favour cluster edges over the bare support. The adsorption of multiple oxygen molecules is not possible on gas-phase anionic clusters, since the adsorption of a single oxygen molecule consumes the extra electron and makes the cluster inactive for further oxygen adsorption¹³⁴. In addition to strong adsorption and activation of oxygen molecules, the perimeter of Au_{14} cluster also dissociates oxygen readily. The calculated barrier is 0.5 eV with respect to the adsorbed oxygen molecule. The final, dissociated state is markedly exothermic by 1.8 eV compared to the initial molecular state and shows a formation of a linear O-Au-O configuration at the edge of the cluster displayed in Figure 15.

A strong thermodynamic driving force for dissociation is seen e.g., for four oxygen

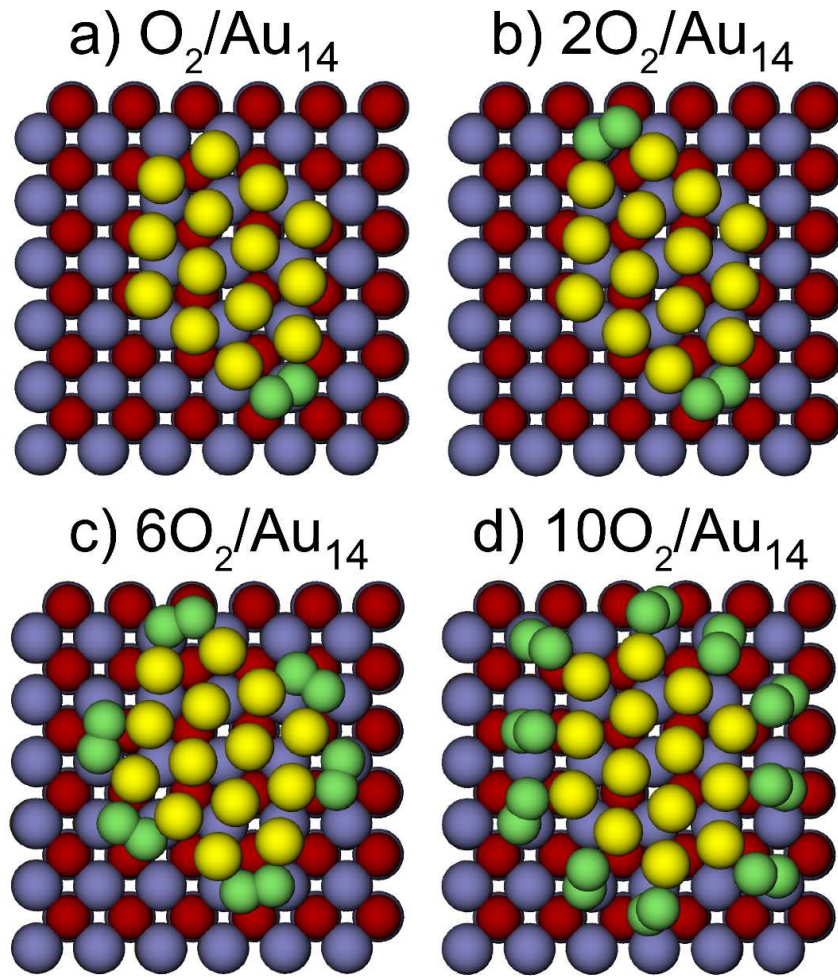


FIG. 14: Optimal adsorption geometries of one, two, six, and ten oxygen molecules on Ag-supported Au_{14} cluster identified in ref.¹¹⁹. Color code: red oxygen in MgO, blue Mo, yellow Au, and green O in O_2 . Figure adapted with permissions from Ref.¹⁹.

molecules, which is exothermic by 1.2 eV /molecule. The binding of atomic oxygen to the perimeter of the cluster leads to a considerable structural distortion of the cluster and formation of linear Au-O-Au chains. The Au atoms in Au-O-Au chains are chemically different, while in the absence of O_2 perimeter Au atoms have excess negative charge of -0.2 to -0.3 $|e|$ in the chains they become positively charged by 0.3 $|e|$. This is further supported by the LDOS analysis showing different electronic structure. All these factors indicate the oxidation of Au atoms in the presence of atomic oxygen. Recent DFT calculations predict Au oxidation at the interface to a TiO_2 support¹³⁵. Conversely, on a bulk Au surface O_2 ad-

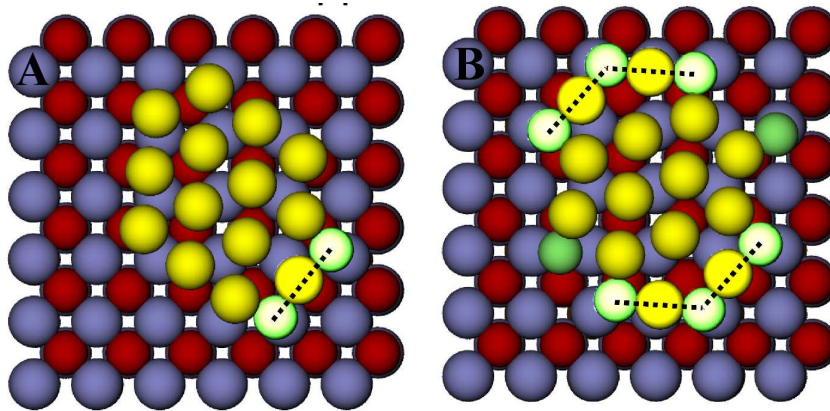


FIG. 15: Optimal adsorption geometries for two and eight O atoms at the perimeter of the Au_{14} cluster supported on $\text{MgO}(2\text{ML})/\text{Ag}(100)$. Color code: red oxygen in MgO , blue Mo, yellow Au, and green O in O_2 . Figure adapted with permissions from Ref.¹⁹.

sorption is endothermic even on low coordinated sites^{94,136} and O_2 adsorption on Au clusters supported on MgO shows weak binding and mildly exothermic dissociative adsorption⁹⁴.

The strong thermodynamic driving force together with the low dissociation barrier, 0.5 eV, renders the dissociation accessible on the supported Au_{14} even at low temperatures. First principles atomistic thermodynamics¹³⁷ was applied to calculate the Gibbs free energy of oxygen adsorption to assess the relative stability of different structures under ambient conditions of oxygen atmosphere. Figure 16 displays free energy plots as a function of O_2 chemical potentials, where temperature and pressure effects were calculated from first principles with appropriate partition functions.

Among the calculated structures $\text{Au}_{14}\text{O}_{8,\text{diss}}$ is thermodynamically the most stable one being nearly 4 eV more favourable than the second best structure, $\text{Au}_{14}\text{O}_{2,\text{diss}}$ at $T=300$ K and O_2 pressure of 1 bar. Metastable bulk and surface forms of gold(III) oxide Au_2O_3 are known to form under special conditions^{138,139}. DFT coupled with atomistic thermodynamics calculations has indicated that atomic oxygen on the Au(111) surface can induce the formation of a two-dimensional gold(I) oxide network as an overlayer on Au(111), predicted to be stable up to 420 K at atmospheric pressure¹⁴⁰.

Sensitivity of oxygen adsorption and activation on a planar or tetrahedral structure of a Au cluster was computationally addressed via Au_{20} supported on a $\text{MgO}(1\text{ML})/\text{Mo}(100)$ surface¹³². In both cases oxygen adsorbs to the perimeter of the cluster at the parallel

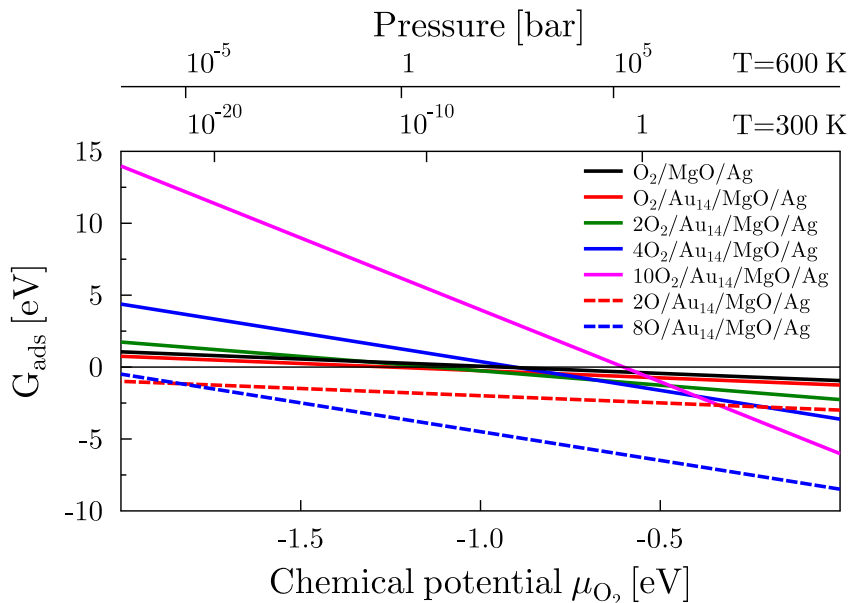


FIG. 16: The free energy of oxygen adsorption, ΔG_{ads} , as a function of oxygen chemical potential, μ_{O_2} . Figure adapted with permissions from Ref. ¹⁹.

configuration, activates to a peroxo state, and dissociates with a barrier of about 0.3 eV with respect to the molecularly adsorbed oxygen. A slight difference of 0.2 eV in O_2 dissociation barrier heights on Au_{14} and Au_{20} potentially originates from different metal supports as oxygen binding on MgO/Mo is stronger than on MgO/Ag , or from different MgO film thicknesses.

CO adsorption has been computationally addressed on Au_{3-7} , Au_{12} , and Au_{22} clusters on MgO/Ag surfaces¹²³. The adsorption energies range from -0.5 to -1 eV depending on the cluster size and are more exothermic than on the bare MgO/Ag surface. CO does not bind to the high coordinated Au atoms of 1D and 2D Au clusters or the central area of the larger islands but favours solely the low-coordinated sites at the edge of these structures forming a tilted orientation at the cluster boundary. Vibrational frequency analysis displays a red-shift of $\sim 50-60 \text{ cm}^{-1}$ in $\omega(CO)$ for MgO/Ag supported Au clusters compared to same clusters on bulk MgO or in gas-phase counterparts. The shift is ascribed to the charge transfer to the cluster agreeing nicely with experimental results, which also indicate that CO exclusively binds to Au atoms at the island perimeter¹⁴¹. Similar to O_2 adsorption, the favouring of low-coordinated boundary sites means that for larger 2D clusters only a minority of Au atoms bind CO ; in addition, CO and O_2 may exhibit mutual competition of these sites.

The formation of adsorbed CO_2 on planar $\text{Au}_{20}/\text{MgO}/\text{Ag}$ is essentially a non-activated process involving a negligible barrier of 0.07 eV according to DFT calculations and the desorption energy of CO_2 is 0.27 eV¹³². Among the calculated barriers, the rate determining step is the dissociation of the molecular oxygen, which is suggested to correspond to the low temperature CO oxidation in experiments¹³². High temperature CO_2 formation was proposed to originate from the reaction of CO with an activated, peripherally adsorbed but undissociated O_2 with an activation energy of 0.66 eV¹³². A completely different reaction mechanism was put forward for bulk MgO supported Au nanoparticles for which calculations suggest that CO oxidation follows an Eley-Rideal mechanism, where CO adsorbs on the nanoparticle and reacts with the coming oxygen molecule with activation energy of ~ 0.2 - 0.4 eV⁹⁴. Similar activation energies are computed on flat Au surfaces⁹⁴ and TiO_2 supported Au_{10} ¹⁰⁰. On defected bulk MgO Au_8 was found to be the smallest cluster capable for CO oxidation with the calculated barrier of 0.5 eV⁸⁸. In conclusion, regardless of the support used in calculations, the activation barriers for CO oxidation have about the same order of magnitude but different reaction mechanisms.

C. Dissociative adsorption of water

Water is the most abundant natural resources and a candidate for generating hydrogen. Under realistic reaction conditions many oxides are hydroxylated in air¹⁴² and surface hydroxyl groups may strongly impact on the chemical characteristics of oxide surfaces¹⁴³. Water dissociation on bulk MgO surfaces has been extensively studied both experimentally and theoretically. Ab initio molecular dynamics has been applied to compare water adsorption on flat and stepped MgO surface at low coverage^{144,145}. The simulations show that water merely physisorbs on bulk MgO(100) while on coordinately unsaturated step sites dissociation takes places readily^{144,145}. All DFT calculations indicate that water dissociation is thermodynamically unfavourable due to fragment separation on MgO(100) at low coverage¹⁴⁶⁻¹⁴⁹, but at 1ML coverage calculations suggest a collective dissociation process such that one third of water molecules break down¹⁵⁰⁻¹⁵². Experimentally, LEED and HAS measurements revealed that water adopts a (3x2) superstructure¹⁵³ and the combined HREELS and UPS study demonstrated a partially dissociated water layer¹⁵⁴. The first experimental studies on submonolayers of water on a MgO/Ag(100) system employing spectroscopic methods

showed evidence of facile hydrolysis^{155–157}, where the active site was proposed to be at the metal-oxide interface. This was further supported by the DFT study of the system¹⁵⁸.

DFT calculations¹⁴⁸ followed by a combined experimental and theoretical study²³ on water adsorption and dissociation on MgO/Ag(100) display many interesting features. Figure 17 compares the optimal adsorption structures of a molecular water on MgO(100) and MgO(2ML)/Ag(100) surfaces. On the metal-supported thin film the oxygen atom of a water molecule is favourably located above a Mg cation, which is in line with STM results,²³ where one hydrogen atom points asymmetrically towards a neighbouring surface anion^{23,148}. The adsorption energy is about -0.5 eV and indicates that the metal support does not enhance the adsorption. Interestingly, calculations predict that in the presence of an Au cluster a water molecule prefers to sit over the oxide to the Au cluster¹⁵⁹. The bottom two figures in Figure 17 depict adsorption structures for a dissociated water on both bare and Ag-supported MgO. Energetics show that water dissociation is endothermic on both cases that is again in agreement with observations in STM measurements. The calculated adsorption geometries of dissociated water differ since on bare MgO both OH and H species reside on top positions and on supported film OH prefers a bridge geometry between two Mg cations.

STM experiments give evidence for two distinct dissociation channels²³ depending on the film thickness. On the 2ML film the dissociation probability increase rapidly when bias and tunneling current dependent threshold energy exceeds 0.48 eV that corresponds the asymmetric O-H stretching mode energy. This strongly supports interpretation that vibrationally induced excitation is responsible for dissociation to OH and H. The MgO film plays a central role to facilitate vibrationally induced dissociation due to decoupling allowed by the insulating MgO film therefore on the 2ML-thick film the dissociation barrier of water is reduced below the energy of the doubly excited ν_{OH} mode. On the 3ML film higher, 1.5 V, bias voltage is needed to initiate dissociation, which is suggested to proceed via electronic excitation forming adsorbed oxygen. This is in line with spectroscopic experiments, which indicate that under low relative humidity conditions water dissociates on 4-5.5 ML thick MgO films at defect sites¹⁶⁰ as predicted also by DFT calculations¹⁴⁸. The DFT calculations reveal the pivotal role of film thickness on barrier height²³, which is about 1 eV on MgO(3ML)/Ag(100) and bare MgO reducing to to 0.56 eV on MgO(1ML)/Ag(100). The presence of under-coordinated step sites impacts substantially as they dissociate water spontaneously on both MgO and MgO/Ag surfaces¹⁴⁸.

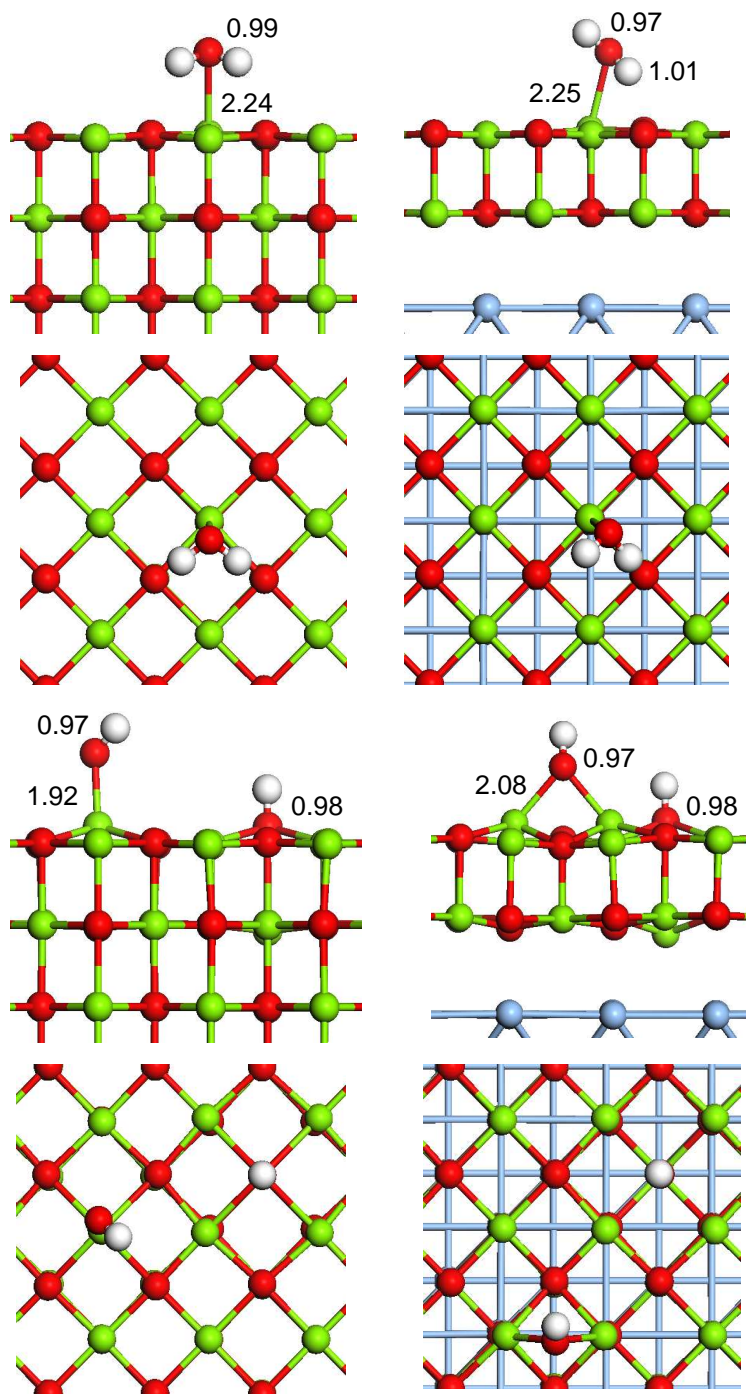


FIG. 17: The most favourable adsorption geometries on MgO(100) and MgO/Ag(100) surfaces. The selected distances are given in angstroms. The colour coding is Ag atoms are blue, Mg atoms green, O atoms red, and H atoms white. Figure adapted with permissions from Ref.¹⁴⁸.

Interestingly, calculations show that isolated H-bonded water dimers facilitate barrierless water dissociation on a bare and Ag-supported MgO(100) surface¹⁶¹. Dissociation is further stabilised on MgO ultra-thin films, which is attributed to two factors. The presence of metal support stabilizes the final state of charged fragments owing to structural relaxations in oxide that induce a strong corrugation of the film. Furthermore, based on the analysis of interaction energies the ion-ion interaction is suggested to change to a dipole-dipole type interaction ensuing a weakly bound ion pair¹⁶¹. At monolayer water coverages different structural motifs corresponding to surface cells with different sizes have been employed in calculations¹⁴⁸. An example applied structural model is given in Figure 18. The optimized structures show that a part of monolayer is dissociated and molecular water adsorbs on Mg²⁺ sites with one H pointing toward OH_{ads}. The adsorption energies are more exothermic by about 0.3 eV/H₂O than those obtained at low coverage. For comparison, on FeO(111)(1ML)/Pt(111) the enhancement in water adsorption is even more pronounced according to calculations since one water molecule barely binds to the substrate, while the presence of the second water molecule stabilizes the average adsorption energy by ~ -0.5 eV¹⁶. In both systems enhanced adsorption is attributed to the formation of strong hydrogen bonds. Recent STM experiments on a water tetramer on NaCl(001)/Au(111) reveal directionality of the hydrogen bonds at the orbital level¹⁶². The calculated fraction of dissociated water molecules is 1/3 on MgO/Ag that is in line with previous calculations on bare MgO^{150,151} and independent of the computational surface cell used. This can be rationalized as follows: Upon dissociation of one water molecule two strong HOH-OH_{ads} bonds are formed (a spare H is at the O-top site) and the number of such bonds is maximized for a dissociation ratio of one-third.

V. MODIFICATIONS AT THE OXIDE-SUPPORT INTERFACE: OXYGEN VACANCIES AND DOPANTS

The properties of metal supported ultra-thin oxide films can be tuned without varying the film thickness via engineering the interface between the metal support and the oxide. This can be achieved by introducing impurity atoms into the metal oxide interface and by varying the species, which in turn has been predicted to modify the electronic characteristics of the system and can be seen as changes in the work function¹⁶³⁻¹⁶⁵. Also, interfacial vacancies can be induced in the supported oxide films. In these systems kinetic effects have been

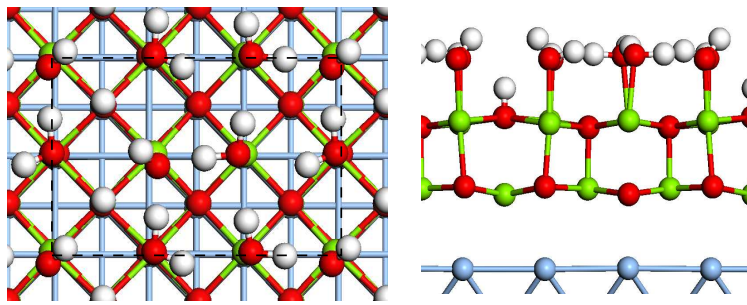


FIG. 18: The structural model of a (3x2) unit cell with a monolayer of water on MgO/Ag(100) from top (left) and side (right). The surface cell is indicated as dashed line and the coloring code is as follows: Ag blue, Mg green, O red, and H white. Figure adapted with permissions from Ref.¹⁴⁸.

identified to be important for reducing vacancies from the buried interface⁷⁰. Figure 19 displays a structural representation of surface, central, and interfacial oxygen vacancies and the interfacial dopant. Recent experimental studies demonstrate how to incorporate Mg atoms to the MgO(100)/Ag(100) interface and identify the mechanism behind the work function decrease ($\Delta\Phi$) during Mg exposure¹⁶⁶. The work function decrease can be, as large as 0.5 eV, attributed to Fermi level pinning and band bending effects. For non-modified MgO/Ag(100) systems measured $\Delta\Phi$ values ranging from 1.1 to 1.4 eV⁶¹ and from 0.7 to 0.8 eV⁵⁵ have been reported; they depend both on film preparation and the method to measure the work function. DFT studies unravel that oxygen vacancies decrease the work function but $\Delta\Phi$ depends sensitively on the charge state and the position of the vacancy⁵², and therefore a direct comparison to experimental value -which is an average value- is difficult.

According to DFT results, oxygen vacancies are preferentially located at the interface between the oxide and the support metal in MgO_{1-x}/Ag and MgO_{1-x}/Mo systems^{42,47,167,168}. The calculated formation energy of the vacancy on the surface of supported MgO is about 6 eV but for an interfacial vacancy it is about 1 eV less^{42,48,167,168}. Therefore in thermodynamic equilibrium, interfacial vacancies constitute the majority of vacancies in the oxide. In this case, an electron is transferred from the vacancy to an underlying metal, creating a singly charged F⁺ center^{47,169}. Calculations show that while regular MgO layers bind weakly to the Ag substrate, the buried vacancies increase the adhesion energy between the metal and the support^{42,47} as shown in Figure 20. The interaction between the regular MgO and Mo is stronger, owing to on one hand the larger covalency contribution of the oxygen anions and

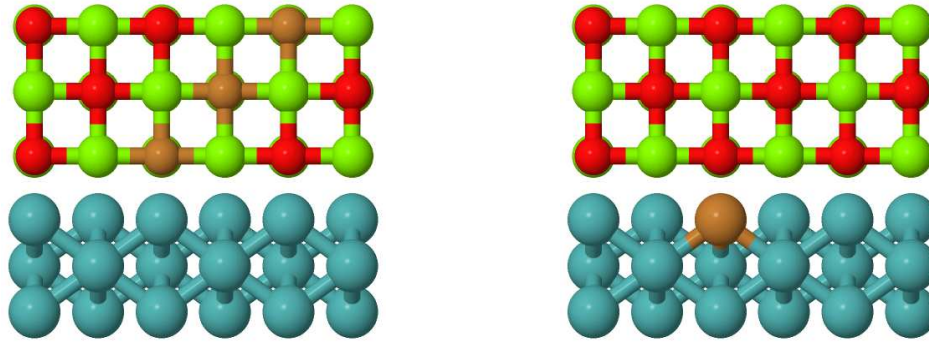


FIG. 19: The schematic representation of an interfacial, central, and surface oxygen vacancy (on the left) and the interfacial impurity atom (on the right) on a metal supported MgO(3ML). Color code: red spheres stand for oxygen, blue is for Mo, green corresponds Mg and brown stands for an impurity or an oxygen vacancy.

Mo (Figure 20) and on the other hand to the increase of the interaction in the presence of an interfacial oxygen vacancy.

The charge state of the interfacial vacancy has been addressed employing different functionals, variable film thickness, and structure models^{47,52,169}. The studies agree that the F^+ center is the most stable defect charge state for the interfacial vacancy. The analysis of structural variations of surrounding ions show a distinct structural response to the vacancy charge state. While negligible distortion is seen around F^0 , the nearest neighbour Mg ions are displaced outward by 7% around the F^+ center and by 13 % around the F^{++} center⁵². The metal-oxide interface can also contain spare Mg and O atoms. The calculated formation energies of interface impurities Mg_{imp} and O_{intr} are only 0.45 eV and 1.49 eV, respectively, highlighting the stabilization effect of the oxide and making them energetically more favourable interfacial defects than oxygen vacancies¹⁶⁸. Moreover, the chemical composition and structure can also be modified by substituting an Ag atom at the topmost layer of the (100) surface with e.g., 3d TM atoms (Sc-Zn). Calculations render these structures thermodynamically favourable for all other atoms except Zn, demonstrating the fact that the MgO film stabilizes the interface dopants³¹. The overall amount of stabilization decreases when moving along in the 3d series from Ti to Zn.

Extensive DFT calculations were employed to investigate the role of an interfacial oxygen vacancy, Mg and O impurity atoms¹⁶⁸, and the 3rd row transition metal dopants³¹ on water

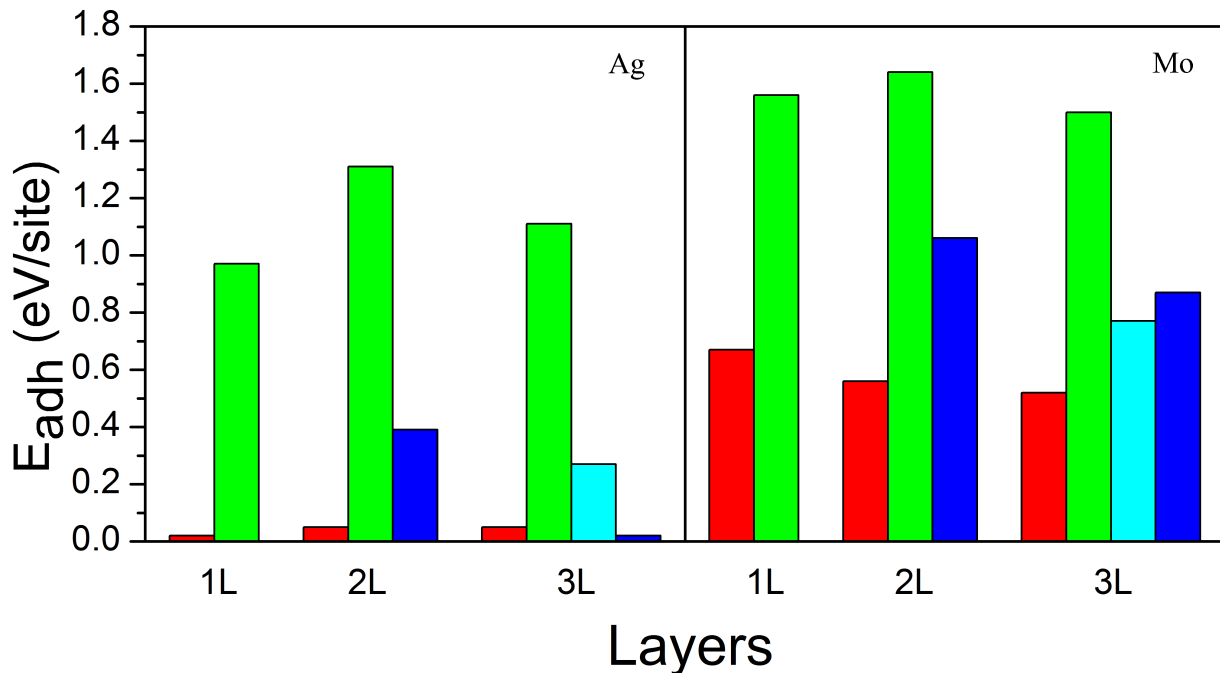


FIG. 20: Panel on the left (right) displays adhesion energy of the MgO film on the Ag(Mo) surface. Color coding: red non-defective film, green stands for an interfacial vacancy, cyan is for a vacancy in the central layer, and blue corresponds the vacancy at the surface. Adhesion energy is calculated as follows for a non-defective film $E_{adh,u} = (E_{MgO/M} - E_{MgO} - E_M)/N$, where N is an interfacial MgO unit and for a defective film as $E_{adh,d} = E_{MgO_{1-x}/M} - E_{MgO_{1-x}} - E_M - NE_{adh,u}$. The positive values indicate exothermic adsorption. Figure adapted with permissions from Ref.⁴⁷.

adsorption and dissociation on Ag-supported MgO. In the latter two cases, an Ag atom in the topmost Ag layer is replaced with either an impurity atom or a dopant atom. The oxide-metal interface modifications change neither the reaction mechanism, nor the adsorption geometries of the water molecule, nor the dissociation products OH^- and H^+ ; they remain similar to those on the ideal $\text{MgO}(100)/\text{Ag}(100)$ surface discussed in chapter IV C. Instead, any kind of the interface defects introduce changes in energetics: smaller for the adsorption energy of water and larger for the transition and final states. The transition state strongly resembles the final state and actually describing it as a transition state is a controversial issue since the H-OH bond is clearly already broken at this state. Comparison of the influence of an interfacial oxygen vacancy and O/Mg impurity atoms shows that the vacancy introduces

the largest stabilization effect: the barrier height drops 42 % compared to the ideal MgO/Ag system. Actually, the dissociation does not require external thermal energy at all to proceed, which means that even a small number of hidden vacancies is sufficient to enhance water dissociation substantially. Among the studied 3d TM dopants, the Ti atom is the most reactive one, and it stabilises the initial, transition and final states by 0.17, 0.51, and 0.48 eV, respectively³¹. This corresponds to the reduction of barrier height by 44 % compared to the ideal MgO/Ag system. The variation of reaction and activation energies show non-linear, double-humped-type behaviour along the 3d TM series, where the second most reactive dopant is iron. The detailed analysis of the doped systems shows that the impurity atom increases adhesion between MgO-Ag as well as rumpling at the interface, but decreases the oxygen-impurity distances. The reactivity and adhesion are correlated in such a way that the stronger adhesion corresponds to higher reactivity. The variation of adhesion energy was shown to reflect the local hybridization between electronic states of the TM dopant and the oxide film and was rationalized with the help of ligand field theory. The extend of d-state splitting of the TM dopant originating from the ligand field of the oxide was shown to fully correlate with the variation of chemical reactivity³¹. The example of water dissociation highlights the fact that a chemical reaction can be controlled by interfacial defects even in the case where the activation of the reactant is not driven by charge transfer. However, the transition state resembles the final state, which consists of charged species.

The second system, for which the influence of interfacial modifications has been computationally studied, is Au adsorption on Mo/Ag supported MgO films in the presence of buried oxygen vacancies. Figure 21 compares Au binding energies on metal-supported ideal and defected MgO films; positive energies refer to exothermic binding. On defected MgO/Ag (Mo) surfaces Au adsorption strength depends on the position of the vacancy in the system: the strongest adsorption is found for a surface vacancy and the weakest for the interface vacancy⁴⁷. While on MgO/Ag(100) Au binding is always stronger on a 2-3 ML thick film with a buried vacancy than on the ideal surface, this is not the case for Mo. The finding indicates that on MgO(100)/Ag(100) gold would preferentially decorate sites with underlying buried vacancies. This offers a possible explanation why isolated Au atoms on MgO/Ag(100) terraces have been identified as almost immobile species in STM images¹⁰⁹. Similar preference is not seen for Mo due to more covalent Mo-oxide anions interaction, which locks the electron density in the interface. The extensive electronic structure analysis

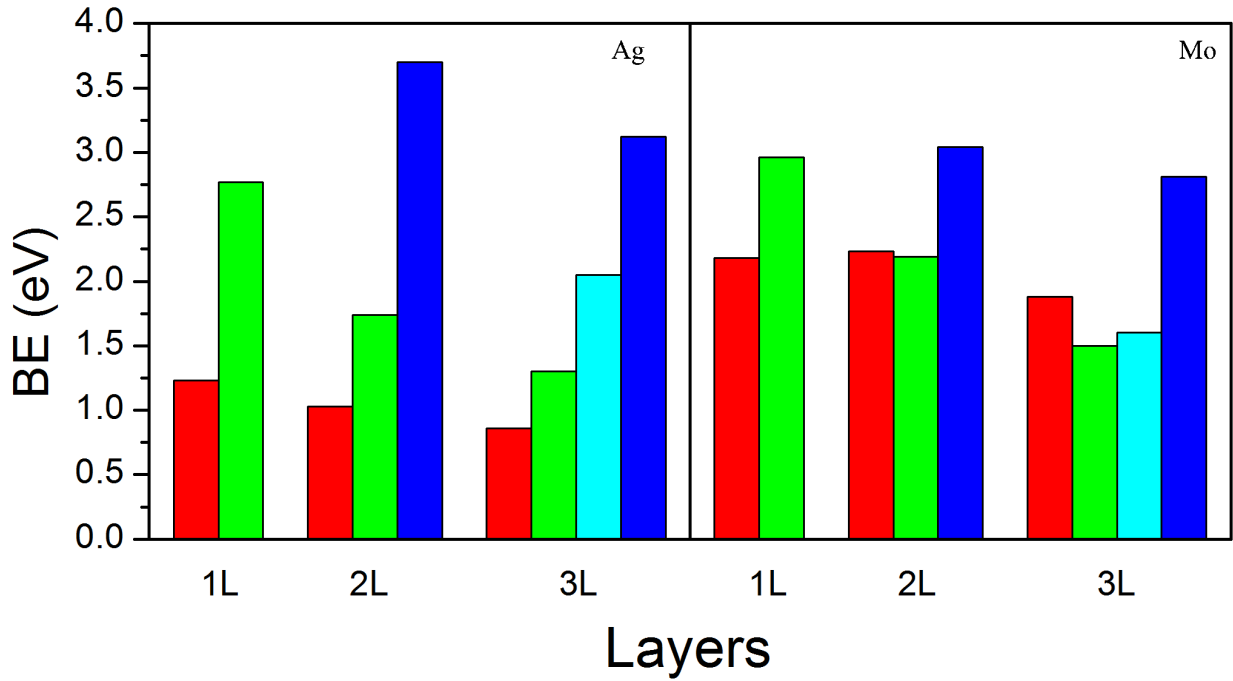


FIG. 21: The binding energy of Au to the Ag (Mo)-supported ultra-thin MgO films in panel a(b). Color coding: red a non-defective film, green an interfacial vacancy, cyan a central-layer vacancy, and blue a surface vacancy. Positive values indicate exothermic adsorption. Figure adapted with permissions from Ref. ⁴⁷.

including the plane average density analysis, the electronic localization function, and the Bader charge analysis, unravel that while one vacancy electron stays in a support metal atom under the vacancy, the second electron goes to a Au atom; thus the vacancy is more like a F^{++} center. The simple thermodynamic analysis -with charge transfer and electrostatic terms- renders the formation of F^{++} thermodynamically possible. According to the calculations, the electron transfer process is independent of the film thickness (at the range of 1-3 layers), and takes place similarly on both Ag and Mo support metals.

The fact that Au binding energy to the surface vacancy is always more exothermic than to the site with a buried vacancy, leads to the thermodynamic driving force to extract the vacancy from the metal-oxide interface to the surface. Despite thermodynamic preference, the vacancy extraction from the interface to the oxide surface can be hindered by kinetic factors, that is, too high diffusion barriers. The diffusion pathway of an oxygen vacancy consists of jumps between two nearest neighbour sites. In bulk MgO this has been reported

to be highly demanding with activation energy of ~ 4.25 eV¹⁷⁰. On two or three layers thick, unsupported MgO slabs the barrier is markedly reduced being still, however, ~ 2.5 eV¹⁶⁷. On 2 or 3 ML thick Mo/Ag supported MgO films the barrier height ranges from 1.7 to 2.6 eV, where the highest barrier corresponds to vacancy diffusion to/from the central MgO layer. DFT calculations show that the presence of an Au adatom strongly reduces diffusion barriers, which means enhanced diffusion by a factor of two at room temperature. Altogether, the calculations suggest that the extraction of oxygen vacancies in ultra-thin MgO films is both thermodynamically and kinetically feasible. To further rationalize the obtained results, the existence of a Brønsted-Evans-Polanyi (BEP) relationship, introduced by Nørskov *et al.*¹³⁶, was tested. The BEP relationship relates an activation energy for a given reaction or an elementary step to its corresponding reaction energy in a linear manner, and provides a way to identify thermodynamic-kinetic dependencies. Numerous DFT studies show how the results fall on the BEP line for different reactions on metal surfaces^{136,171–174} and nanoparticles¹⁷⁵, and for diffusion processes in oxide systems^{170,176}. In the present case, plotting the activation energy for oxygen vacancy diffusion as a function of the energy difference between two vacancy positions, two BEP-type of relationships appear (Figure 22) and the direction of the diffusion is from the support toward the adsorbate. The observed two lines arise from high barrier values corresponding to vacancy diffusion in MgO_{1-x}/Ag and MgO_{1-x}/Mo, and from lower values for Au/MgO_{1-x}/Ag and Au/MgO_{1-x}/Mo systems. The reasons behind two BEP lines can be understood by analyzing the transition states for vacancy diffusion. The ELF (electron localization function) and Bader analysis for diffusion pathways give a constant, 2e charge for moving oxygen, while the charge left into the vacancy depends on the system. It is one unit charge for the F⁺-like defect in MgO/Ag and MgO/Mo systems and zero for F⁺⁺ in Au/MgO_{1-x}/Ag and Au/MgO_{1-x}/Mo. The activation energy, that is the energy difference between the initial and transitions state, is solely determined by electrostatic terms, which on the other hand depend on the vacancy position and the distances between charged species. Thus, the appearance of the two BEP lines implies two differently charged species.

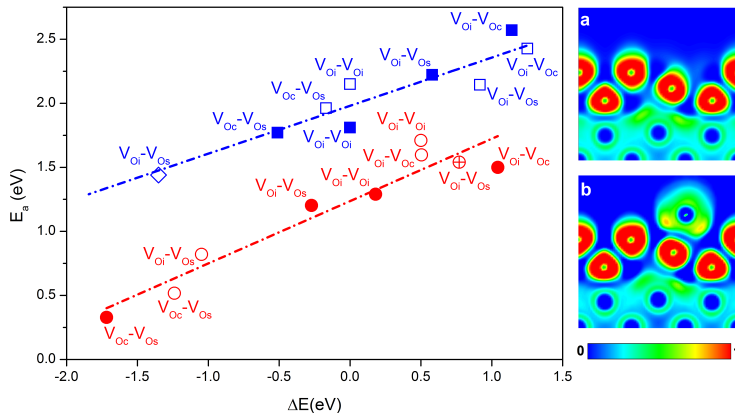


FIG. 22: Left: a Brønsted-Evans-Polanyi plot. Energy barrier for diffusion, E_a , as a function of the energy difference between two vacancy positions, ΔE . Blue (red) symbols correspond to (Au)/MgO/M, and open (filled) symbols stand for Ag (Mo). The thickness of the MgO film varies from one to three monolayers. The crossed circles refer to vertical diffusion far away from Au in the Au/MgO(2ML)/Ag system. V_{oi} stands for an interfacial vacancy, V_{oc} corresponds a vacancy in the center of the slab, and V_{os} is a vacancy at the surface. Right: panels a and b display ELF (electron localization function) plots for the transition states with and without Au on the MgO(2ML)/Ag substrate, respectively. Figure adapted with permissions from ref. ⁴⁷.

VI. DOPING

Metal-supported simple oxide systems can be understood as an extreme case of doped oxides having high concentration of extra electrons detectable in STM measurements. In principle, a dopant has a similar effect as it can provide extra electrons into the oxide. However, in doped oxides the concentration of spare electrons is lower than in supported films and they are also more localized. Furthermore, the distribution of these electrons might be uneven. Altogether, this means that understanding the properties of doped oxides is challenging but the knowledge gained from metal-supported thin-film systems give insight on the characteristics of doped oxides. Calculations help to determine the composition and morphology of oxide material since those are highly challenging to experimentally resolve under working conditions. Simple ionic oxides are auspicious materials to probe the modifications introduced by dopants to characteristics of a host oxide. Possible dopant atoms

can be divided into two groups: guest cations capable of providing less electrons than the host cations and those that can provide more. Note, that one can not neglect the role of the host oxide either: e.g., CaO is more reactive than MgO because of its larger lattice parameter and the smaller Madelung potential. Moreover, its band gap is smaller and ions more polarizable. According to DFT calculations, transition metal dopants Mo and Cr adopt a formal 2+ charge state in an ideal and neutral MgO and CaO slabs, reproducing the nature of a host cation³⁸. STM experiments on the other hand reveal, that it is possible to induce charging and discharging of a Mo dopant sitting at the vicinity of the CaO surface with a STM tip, hence making Mo³⁺ cations¹⁷⁷. The presence of high valent dopants can also introduce structural modifications to an oxide matrix, as they are known to increase the number of cation vacancies. This is clearly seen in DFT calculations, where the vacancy formation energy drops from 8 eV to 1 and 1.7 eV for MgO_{Cr} and CaO_{Mo}, respectively, and leads to a loss of another electron to a host oxide³⁸. This, naturally, has implications to other possible electron transfer processes. Topographic STM images unambiguously show, that high valent TM substitute doping of CaO leads to the formation of 2D Au islands³⁷, similar to a metal supported ultra-thin oxide film. DFT calculations highlight the enhanced binding of an Au atom on Mo-doped CaO with adsorption energy nearly three times as large as computed on the ideal CaO surface, despite the absence of a direct contact between the Au and dopant atoms³⁷. On pristine CaO, the Au is preferentially located on the oxygen ion with adsorption energy of -1.35 eV, while the adsorption energy as large as -3.90 (-3.50) eV is found when the Mo dopant is in the second (third) layer directly below the adsorbate. The enhanced bonding was ascribed to charge transfer from Mo to Au, leading to strong electrostatic interactions and concomitant lattice relaxations near the dopant³⁷. Additional DFT studies were performed to understand the thermodynamic factors determining Au adsorption energy on high-valence doped CaO⁴⁰.

To rationalize the variation of adsorption strength as a function of a Au-dopant distance, we employed the concept of acid-base interaction, where a high-valence dopant Mo acts as a base donating charge and Au is the acid accepting charge⁴⁰. In these calculations, the 10 ML:s layer-thick slab was used and the dopant was placed into the 3'rd layer or deeper leaving at least 2 ML of ideal CaO for a protective capping as in experiments³⁷. While DFT studies in both references show that Au favours adsorption on an oxygen anion being neutral, Andersin *et al.* reported that, according the Bader charge analysis, an Au atom

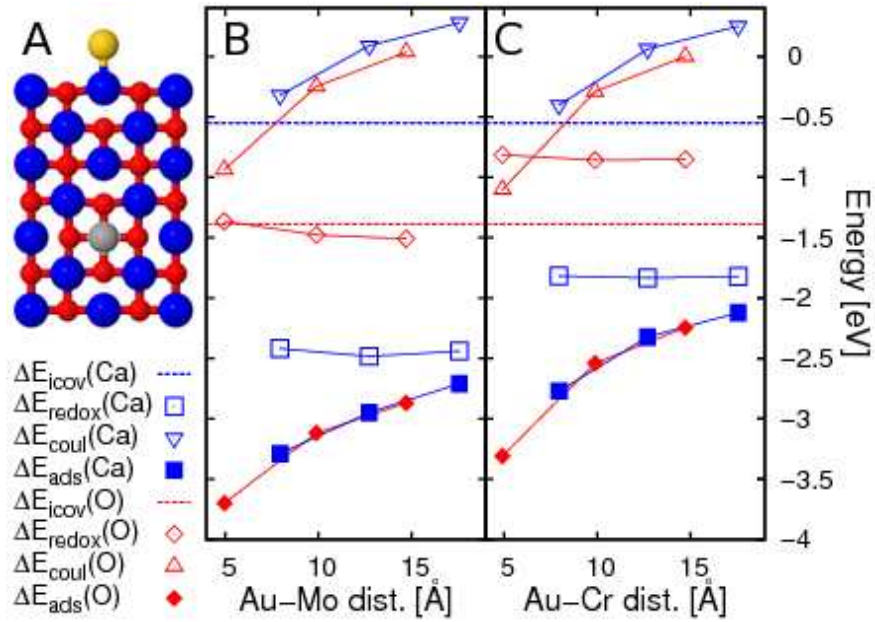


FIG. 23: A) displays the side view of the 7 topmost layers of 10 ML layer thick computational unit cell, which was used to model Au adsorption on TM-doped CaO. The color coding as as follows blue stands for Ca atoms, red is for oxygens, while yellow and gray are for a Au atom and a dopant, respectively. Panels B) and C) The adsorption energy of a Au atom as a function of dopant depth together with the different energy contributions.

Figure adapted with permissions from Ref. ⁴⁰.

becomes negatively charged on a Ca-site over an pristine CaO(100). Moreover, the PDOS analysis reveals that both 6s spin levels become occupied together with vanishing magnetic moment, but the adsorption energy of Au is only -0.55 eV, which is ~ 0.8 eV less exothermic than found for Au on the O-top site. These results indicate that charging of Au cannot alone be responsible for the increase in adsorption energy upon doping the oxide. Au adsorption was further analyzed employing a Born-Haber cycle, where the Au-CaMoO interaction is broken down to the three contributions shown in Fig. 24.

The first contribution is a direct iono-covalent interaction between the Au and the surface ion on the pristine CaO, which involves direct orbital overlapping and charging on the top of Ca-atom. The energy change related to this term is called ΔE_{icov} . The Au-dopant interaction is divided into two terms: (a) the redox process between the Au and the dopant (ΔE_{redox}) containing an electron transfer from the overvalent dopant to the Au atom and (b)

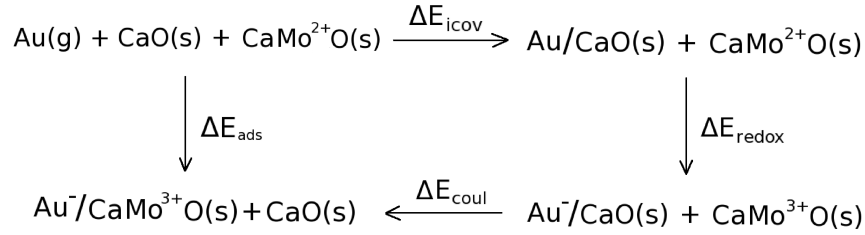


FIG. 24: The Born Haber cycle for Au adsorption on Mo-doped CaO. Au adhesion on the substrate (=adsorption energy ΔE_{ads}) is divided into three contributions: ΔE_{icov} stands for the iono-covalent bonding of a Au atom onto the pristine CaO surface, ΔE_{redox} is the redox interaction between Au and Mo leading to charge species infinitely far apart, and ΔE_{coul} corresponds the screened electrostatic interaction between Au and Mo.

Figure adapted with permissions from Ref. 40.

the electrostatic interaction between the Au^{-1} and a positively charged dopant ΔE_{coul} . Figure 23 B) and C) display adsorption energies together with above-described site-dependent contributions on both Mo- and Cr-doped surfaces as a function of the Au-dopant distance. Clearly, adsorption becomes weaker with the increasing distance between the Au and the dopant. The term ΔE_{coul} demonstrates approximately $1/r$ behaviour, where r is the Au-dopant distance proving further support that energy change ΔE_{coul} describes electrostatic interaction. Owing to strong screening by the polarized oxide, the Coulomb interaction is significant only at very short distances. In experiments the capping region is typically a few undoped CaO layers³⁷. If the Mo is in the third layer the Au-Mo distance is approximately 8 Å which corresponds the contribution of only ~ -0.5 eV while the adsorption energy is -3.0 eV, thus the electrostatic contribution to Au adsorption is minor on this oxide. The adsorption energy is dominated by the other two terms. The iono-covalent term is independent of a dopant as it describes the interaction between Au and ions in the oxide matrix but depends on the adsorption site. The ΔE_{redox} term represents energy gain related to the electron exchange between Au and the dopant and corresponds to the dominant energy contribution in adsorption energy. It can be divided into two cases. Since the Au gains charge already upon the adsorption on a Ca-site of pristine CaO, the redox energy change is assigned to the system stabilization due to Mo oxidation as the more cationic dopant binds stronger

to anionic O^{2-} . This is manifested as decreased distance between the dopant and the surrounding oxygens. Since this is a local effect, it does not depend on the depth of the dopant as seen in Figure 23. On an O-top site Au is initially neutral and thus the redox process includes charge transfer and stabilization due to structural relaxations around the dopant; again, the redox energy saturates quickly to a constant value. The redox energies differ by 1 eV such that the less exothermic value is found for the O-top site. This is due to Coulomb repulsion between negatively charged Au and negatively charged O, manifested also in a Au-O bond length, which increases $\sim 0.6 \text{ \AA}$ upon Au charging. Figures 23 B) and C) show that the above discussion is independent of the dopant as both Mo and Cr display similar behaviour. The comparison of Au adsorption energies on Mo and Cr doped CaO surfaces show smaller stabilization on the Cr-doped than on the Mo-doped surface. The difference is ascribed to smaller redox energy on CaO_{Cr} . While according to the Bader charges and magnetic moments Cr donates altogether 3 electrons (2 to the oxide and 1 to the Au) and geometric differences are minor, the smaller redox energy originates from higher 3rd ionization energy. Actually, on the ideal CaO surface the redox energy correlates with ionization energies of different high-valent transition metal dopants near Mo and Cr in the periodic table as illustrated in Figure 25. The higher the 3rd ionization energy, the less exothermic is the redox energy, which indicates that the cost of electron removal from the dopant increases with increasing ionization energy. In real systems, the ideal correlation shown in Figure 25 is not achievable due to the presence electron traps, such as cation vacancies, that compete with adsorbates for electrons. In addition, the host oxide can affect electron transfer unfavourably via crystal field splitting, which stabilizes the donor states too much and hampers the electron transfer¹⁷⁸. Calculations show that on a Mo^{3+} -MgO surface with one cation vacancy the adsorption is only 0.2 eV more exothermic than on pristine MgO, whereas 0.75 eV energy difference is seen between Mo^{3+} -CaO and CaO systems⁷². Molecular oxygen is also a strong acid and thus it is not surprising that enhanced binding on Mo-doped CaO is demonstrated in STM experiments, which is further supported by DFT calculations featuring 0.8 eV increase in O_2 adsorption energy and the formation of a superoxo species¹⁷⁹. The Born-Haber cycle analysis for O_2 renders the redox energy as a main contribution in adsorption energy on Mo-doped CaO¹⁸⁰. While DFT calculations have so far mainly focused on high-valence doped MgO and CaO systems, understanding undervalent doped oxides is also essential. Particularly important is Li-doped MgO, which is an active catalyst for ox-

idative coupling of methane³⁴. The reaction has not been thoroughly understood yet and for example, an active site for a homolytic CH₃-H bond breaking step has remained elusive. In the case of undervalent doped systems, the Born-Haber cycle analysis can also be applied to unravel the relevance of different energy terms for e.g., Au adsorption, which has been experimentally studied³⁹. STM experiments show that depending on Li concentration on Mo-doped CaO the Au growth mode is either 2D or 3D. On bare and Li-doped CaO, Au aggregates favour 3D structures whereas on Mo-doped 2D structures are preferred³⁹. The observed changes can be explained with electron transfer from a dopant to a Au particle, which takes place on Mo-doped CaO but which is not possible on bare or Li-doped CaO. Adding Li to Mo-doped CaO will neutralize the impact of a Mo dopant and prevent the charge transfer from Mo to Au.

The combined STM-DFT study illustrates that charge transfer strongly depends on the nature of a dopant and an oxide: while Au becomes negatively charged on Mo-doped CaO it stays neutral on Cr-doped MgO. This is manifested in the growth mode of Au, which is 2D for charged species and 3D for neutral ones³⁸. Addition of Li dopants to Mo-doped CaO leads to decrease in fraction of 2D Au islands with respect to 3D aggregates indicating that electron transfer happens from Mo to Li atoms and not to adsorbed Au³⁹. The shape of an Au cluster has been computationally addressed on Al-doped MgO, where planar and tetrahedral Au₂₀ configurations were compared¹⁸¹. Calculations demonstrate that with increasing dopant concentration the binding energy of a cluster increases. The binding energy depends on the position of the dopant being more exothermic when the dopant is in the second layer of the oxide and under the cluster. In all studied dopant concentrations a planar geometry is more favourable than the tetrahedral one and the energy difference between these two geometries depends linearly on dopant concentration displaying a larger difference at higher concentrations. The electronic structure analysis shows substantial charge transfer from the substrate to the cluster, which also increases with increasing dopant concentration.

The comparison of Au adsorption energies on doped MgO and CaO surfaces calculated with different functionals (PBE, PBE0, HSE0 and PBE+U) shows that absolute values of adsorption energies are functional dependent but charge transfer trends are similar in all cases. On Cr²⁺-MgO and Mo²⁺-CaO Au becomes negatively charged, whereas on Cr³⁺-MgO it stays neutral⁷². To separate the role of a guest cation from that of the oxide, Au adsorption on two selected surfaces namely Mo³⁺-MgO and Cr³⁺-CaO were calculated. The

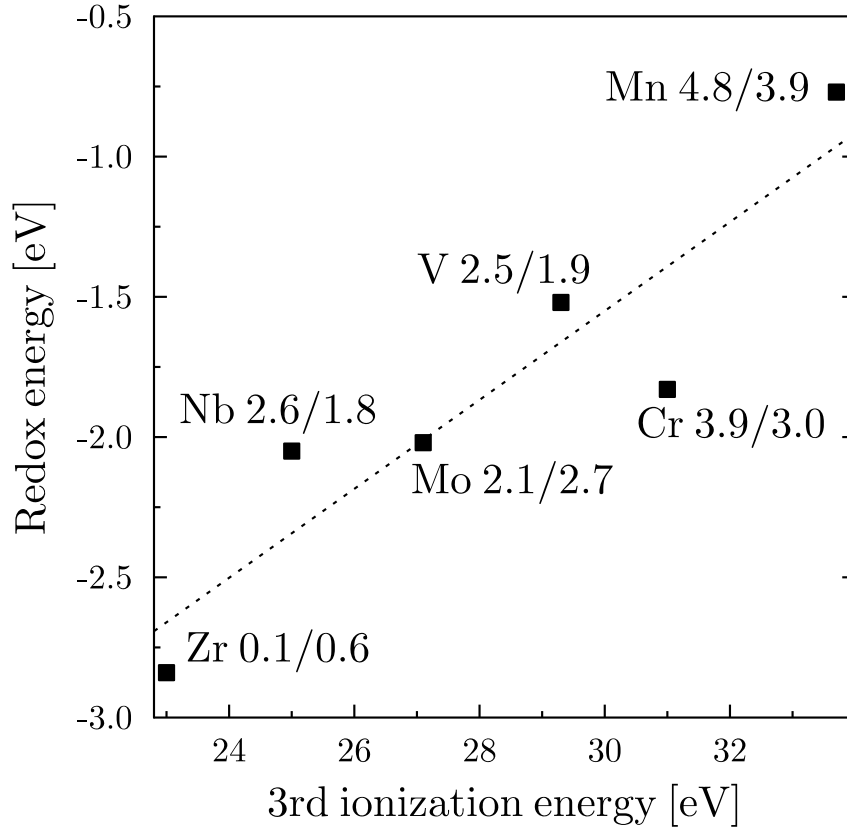


FIG. 25: The calculated redox energy in the TM-doped CaO(100) surface as a function of the measured 3rd ionization energy of the different dopants. The notations $\mu(2+)$ and $\mu(3+)$, given after the name of the element, refer to the magnetic moments of double and triple cations of the dopants, respectively. Figure adapted with permissions from Ref. ⁴⁰

results show that even in CaO Cr³⁺ is unable to donate an electron to Au regardless of smaller crystal field splitting leading to favourable position of donor states. For comparison, Au becomes negatively charged on Mo³⁺-MgO as well as on Mo³⁺-CaO. All these together further support the suggestion⁴⁰ that ionization energy, which stands for the cost of oxidation of the TM ion, determines the dopant's efficiency to transfer an electron to an acceptor in the system.

VII. CONCLUSIONS

Over the past years significant advances have been made in the preparation and experimental studies of tailored oxides as well as in the modeling their properties. These modified oxides have emerged as materials with unique properties, not encountered in their bulk counterparts. The selected examples discussed highlight the potential of simple oxides. They can be made chemically active and can operate as active catalysts or act as supports for catalyst particles. Two different schemes to modify the properties of simple oxides are addressed, namely growing oxides as ultra-thin films over metal supports and doping them with metal impurities. The discussion mainly focuses on theoretical studies for metal supported MgO films and in doped oxides on CaO and MgO systems, while other oxides are occasionally brought in attention for comparison. All the reviewed systems underline the potential and importance of density functional theory calculations and their role to unravel experimentally seen features but even more importantly to predict material properties, especially activity. Despite the fact that computational methods have their limitations, for certain cases, such as buried vacancies, they are almost irreplaceable in addressing the characteristics and impact of hidden defects on adsorption.

The key adsorbates elaborated include electronegative species such as Au atoms and clusters, molecular oxygen, and NO_2 . The adsorption and dissociation of molecular oxygen is considered both on a bare metal-supported ultra-thin MgO and on an Au cluster over Ag-supported MgO. Interestingly, the calculations predict that the presence of the support metal facilitates simultaneous activation of several oxygen molecules. The adsorption and dissociation of non-electronegative water on ideal MgO/Ag is discussed both at low and high water coverages. In the latter case, the formation of strong hydrogen-hydrogen bonds leads to dissociation of a fraction of adsorbed water molecules. In addition, the modifications at the oxide-support interface are addressed in the two cases; on Au adsorption on a MgO/Ag(Mo) surface with an interfacial oxygen vacancy and water adsorption on MgO/Ag with an interfacial dopant. The role of thin-film systems is not limited to model systems but they have a variety of applications including catalysis, solid oxide fuel cells, gas sensors, corrosion protection, and biocompatible materials, just to mention a few. The spectrum and composition of oxide materials developed for different application is broad; some of these oxides are simple while there is an increasing number of fairly complex oxides. In the

future, we need to compute the electronic structure of these complex oxides reliably, which potentially have a variety of different defects, and simultaneously get a description for weak van der Waals interactions. In particular, calculation of line defects increases the system size, which in turn poses challenges for calculations.

On doped CaO and MgO oxides, the adsorption of an Au atom and an O₂ molecule is discussed. While the film thickness is an adjustable parameter in metal-supported thin film systems, in doped oxides the corresponding parameter is the dopant concentration. Moreover, unlike the metal support, dopants can be mobile and they are also predicted to introduce vacancies into oxide. However, calculations indicate that the impact of over-valent dopants on electronegative adsorbates such as Au atoms and O₂ molecules, is similar to the metal support. Thus adsorption is enhanced, the species become negatively charged, and on both supports Au clusters favour planar geometries. With the help of the Born-Haber cycle the enhanced binding is attributed to energy gain owing to simultaneous electron transfer and lattice relaxations. In an idealized system, the ionization energy of the TM dopant explains the variation of Au adsorption energy from one dopant to the other but in reality dopant induced vacancies have an influence on electron transfer processes and modify this ideal rule. While in metal-supported ultra-thin oxide films systems one can gain better control over structural and electronic characteristics, the atomic structure of doped oxides displays larger plasticity and uncertainty. The model system studies of these materials make the basis to identify the key factors determining the function of the material, which paves the way for examination of less-defined oxides.

Doped oxides also have a variety of applications ranging from catalysis and photovoltaic to chemical sensing, solid oxide fuel cells, and coatings. In many cases the doped oxide is in the thin-film arrangement. The presence of dopants typically affects a number of point defects, such as oxygen vacancies, which then strongly impact on surface chemistry of an oxide. From the theoretical point of view, the concentration and distribution of dopants and vacancies substantially enhance the computational burden and add complexity. Although possible, special care must be taken when the Born-Haber cycle is applied to rationalize chemical reactions on complex, doped oxide surfaces. This is because sufficiently accurate description of the electronic structure is needed and because the impact of vacancies must be included to the analysis. Furthermore, the identification of an active site is usually more demanding than on metal surfaces and nanoparticles owing to a larger number of different

factors such as dopant and vacancy concentration, which might influence the nature and characteristics of the active site. One more thing that makes DFT calculations particularly challenging, is the lack of experimental methods, that could reveal the morphology and composition of oxides under reaction conditions. Therefore, there is an urgent need to develop computational methods and concepts to simulate oxide characteristics and establish their key descriptors to advance in one of the most challenging areas of Material Science.

VIII. ACKNOWLEDGEMENTS

I would like to thank my colleagues, collaborators and former and present PhD students and post docs including in particular Prof. H. Häkkinen, Prof. A. Hellman, Prof. H. Grönbeck, Prof. H.J. Freund, Dr. P. Frondelius, Dr J. Andersin, Dr L. Bellarosa and MSc J. Nevalaita. Dr A. Clayborne and Dr V. Apaja are acknowledged for carefully reading the manuscript. The computing resources provided by CSC -IT Center for Science (Espoo) and Nanoscience Center in the University of Jyväskylä, and financial support from the Academy of Finland are greatly acknowledged.

-
- ¹ V. Heinrich, P. Cox, *The surface science of metal oxides*, Cambridge university press, 1994.
 - ² D. Woodruff (Ed.), *The chemical physics of solid surfaces*, volume 9, oxide surfaces, Elsevier, 2001.
 - ³ M. Ganduglia-Pirovano, A. Hofman, J. Sauer, *Surf. Sci. Rep.* 62 (2007) 219.
 - ⁴ H. J. Freund, H. Kuhlenbeck, V. Staemmler, *Rep. Prog. Phys.* 59 (1996) 283–347.
 - ⁵ H. J. Freund and G. Pacchioni, *Chem. Soc. Rev.* 37 (2008) 2224–2242.
 - ⁶ N. Nilius, *Surf. Sci. Rep.* 64 (2009) 595–659.
 - ⁷ L. Giordano, G. Pacchioni, *Acc. Chem. Res.* 44 (2011) 1244.
 - ⁸ G. Pacchioni, H. Freund, *Chem. Rev.* 113 (2013) 4035.
 - ⁹ S. Schintke, S. Messerli, M. Pivetta, F. Patthey, L. Liboulle, M. Stengel, A. D. Vita, W. Schneider, *Phys. Rev. Lett.* 87 (2001) 276801.
 - ¹⁰ C. Lamberti, E. Groppo, C. Prestipino, S. Casassa, A. M. Ferrari, C. Pisani, C. Giovanardi, P. Luches, S. Valeri, F. Boscherini, *Phys. Rev. Lett* 91 (2003) 046101.

- ¹¹ X. Shao, P. Myrach, N. Nilius, H.J. Freund, *J. Phys. Chem. C* 115 (2012) 8784.
- ¹² G. Kresse, M. Schmid, E. Napetsching, M. Shishkin, L. Köhler, P. Varga, *Science* 308 (2005) 1440.
- ¹³ A. Hellman, H. Grönbeck, *Phys. Rev. Lett.* 100 (2008) 116801.
- ¹⁴ Y. Sun, Z. Qin, M. Lewandowski, E. Carrasco, M. Sterrer, S. Shaikhutdinov, H. Freund, *J. Catal.* 266 (2009) 359.
- ¹⁵ Y. N. Sun, L. Giordano, J. Goniakowski, M. Lewandowski, Z. H. Qin, C. Noguera, S. Shaikhutdinov, G. Pacchioni, H. J. Freund, *Angew. Chem. Int. Ed* 49 (2010) 4418.
- ¹⁶ F. Ringleb, Y. Fujimori, H. F. Wang, H. Ariga, E. Carrasco, M. Sterrer, H. Freund, L. Giordano, G. Pacchioni, J. Goniakowski, *J. Phys. Chem. C* 115 (2011) 19328.
- ¹⁷ Y. D. Kim and T. Wei and D. W. Goodman, *Langmuir* 19 (2003) 354.
- ¹⁸ S. Surnev, A. Fortunelli, F. P. Netzer, *Chem. Rev.* 113 (2013) 4314.
- ¹⁹ P. Frondelius, H. Häkkinen, K. Honkala, *Angew. Chem. Int.* 49 (2010) 7913.
- ²⁰ A. Hellman, S. Klacar, H. Grönbeck, *J. Am. Chem. Soc.* 131 (2009) 16636.
- ²¹ Y. Lei, Y. M. Lewandowski, Y. Fujimori, Y. Martynova, I. M. N. Groot, R. J. Meyer, L. Giordano, G. Pacchioni, J. Goniakowski, C. Noguera, S. Shaikhutdinov, H.J. Freund, *ChemCatChem* 3 (2011) 671–674.
- ²² H. Y. T. Chen, L. Giordano, G. Pacchioni, *J. Phys. Chem. C* 117 (2013) 10623.
- ²³ H.J. Shin, J. Jung, K. Motobayashi, S. Yanagisawa, Y. Morikawa, Y. Kim, M. Kawai, *Nat. Mat.* 9 (2010) 442.
- ²⁴ J. Repp, G. Meyer, F.E. Olsson, M. Persson, *Science* 305 (2004) 493.
- ²⁵ L. Gross, F. Mohn, P. Liljeroth, J. Repp, F. J. Giessibl, G. Meyer, *Science* 324 (2009) 1428.
- ²⁶ L. Gross, F. Mohn, N. Moll, P. Liljeroth, G. Meyer, *Science* 325 (2009) 1110.
- ²⁷ K. Muller, D. Torres, J.B. Park, P. Liu, D. Stacchiola, D. E. Starr, *J. Phys. Chem. C* 117 (2013) 280–287.
- ²⁸ G. Pacchioni, L. Giordano, M. Baistrocchi, *Phys. Rev. Lett.* 94 (2005) 226103.
- ²⁹ M. Sterrer, T. Risse, U. M. Pozzoni, L. Giordano, M. Heyde, H. P. Rust, G. Pacchioni, H.J. Freund, *Phys. Rev. Lett.* 98 (2007) 096107.
- ³⁰ L. Giordano, U. Martinez, S. Siculo, G. Pacchioni, *J. Chem. Phys.* (2007) 144713.
- ³¹ J. Jung, H. Shin, Y. Kim, M. Kawai, *J Am. Chem. Soc* 134 (2012) 10554–10561.
- ³² H. Metiu, S. Chretien, Z. Hu, B. Li, X.Y. Sun, *J. Phys. Chem. C* 116 (2012) 439.

- ³³ E. W. McFarland, H. Metiu, *Chem. Rev.* 113 (2013) 4391–4427.
- ³⁴ C. Hammond, S. Conrad, I. Hermans, *ChemSusChem* 5 (2012) 1668–1686.
- ³⁵ M. Gharibi, F. T. Zangeneh, F. Yaripour, S. Sahebdehfar, *Appl. Catal. A* 443–444 (2012) 8–26.
- ³⁶ S. Arndt, G. Laugel, S. Levchenko, R. Horn, M. S. M. Baerns, R. Schlögl, R. Schomäcker, *Catal. Rev. Sci. and Eng.* 53 (2011) 424.
- ³⁷ X. Shao, S. Prada, L. Giordano, G. Pacchioni, N. Nilius, H. J. Freund, *Angew. Chem. Int. Ed.* 50 (2011) 11525–11527.
- ³⁸ F. Stavale, X. Shao, N. Nilius, H. J. Freund, S. Prada, L. Giordano, G. Pacchioni, *J. Am. Chem. Soc.* 134 (2012) 11380.
- ³⁹ X. Shao, N. Nilius, H. J. Freund, *J. Am. Chem. Soc.* 134 (2012) 2532.
- ⁴⁰ J. Andersin, J. Nevalaita, K. Honkala, H. Häkkinen, *Angew. Chem. Int. Ed.* 52 (2013) 1424.
- ⁴¹ L. Giordano, J. Goniakowski, G. Pacchioni, *Phys. Rev. B* 67 (2003) 045410.
- ⁴² N. Lopez, S. Valeri, *Phys. Rev. B* 70 (2004) 125428.
- ⁴³ P. Frondelius, H. Häkkinen, K. Honkala, *New. J. Phys.* 9 (2007) 339.
- ⁴⁴ S. Benedetti, H. M. Benia, N. Nilius, S. Valeri, H. J. Freund, *Chem. Phys. Lett.* 430 (2006) 330.
- ⁴⁵ S. Benedetti, P. Torelli, S. Valeri, H. M. Benia, N. Nilius, G. Renaud, *Phys. Rev. B* 78 (2008) 195411.
- ⁴⁶ K. P. McKenna and A. L. Shluger, *Nat. Mater.* 7 (2008) 859.
- ⁴⁷ L. Bellarosa, N. Lopez, K. Honkala, *J. Phys. Chem. C* 117 (2013) 23806.
- ⁴⁸ K. Honkala, H. Häkkinen, *J. Phys. Chem. C* 111 (2007) 4319.
- ⁴⁹ C. Giovanari, A. di Bona, T. S. Moia, S. Valeri, C. Pisani, M. Sgroi, M. Busso, *Surf. Sci.* 505 (2002) L209–L214.
- ⁵⁰ P. Luches, S. D’Addato, S. Valeri, E. Groppo, C. Prestipino, C. Lamberti, F. Busso, *Phys. Rev. B* 69 (2004) 045412.
- ⁵¹ P. Guenard, G. Renaud, B. Villette, *Phys. B Condens. Matter.* 221 (1996) 205–209.
- ⁵² S. Ling, M.B. Watkins, A.L. Shluger, *J. Phys. Chem. C* 117 (2013) 5075.
- ⁵³ J. Goniakowski, C. Noguera, *Phys. Rev. B* 79 (2009) 155433.
- ⁵⁴ T. Koenig, G. H. Simon, H.-P. Rust, G. Pacchioni, M. Heyde, H.-J. Freund, *J. Am. Chem. Soc.* 131 (48) (2009) 17544–17545.
- ⁵⁵ T. Jaouen, G. Jezequel, G. Delhaye, B. Lepine, P. Turban, P. Schieffer, *Appl. Phys. Lett.* 100

- (2012) 022103.
- ⁵⁶ M. T. Greiner, L. Chai, M. G. Helander, W. M. Tang, Z. H. Lu, *Adv. Funct. Mater.* 22 (2012) 4557–4568.
- ⁵⁷ J. Goniakowski, C. Noguera, *Interface Sci.* 12 (2004) 93.
- ⁵⁸ L. Giordano, G. Pacchioni, *Phys. Chem. Chem. Phys.* 8 (2006) 3335.
- ⁵⁹ L. Sementa, G. Barcaro, F. R. Negreiros, I. O. Thomas, F.P. Netzer, A. M. Ferrari, A. Fortunelli, *J. Chem. Theory Comput.* 8 (2012) 629–638.
- ⁶⁰ S. Prada, U. Martinez, G. Pacchioni, *Phys. Rev. B* 78 (2008) 235423.
- ⁶¹ T. König, G. H. Simon, H. P. Rust, M. J. Heyde, *J. Phys. Chem. C* 113 (26) (2009) 11301–11305.
- ⁶² T. Jaouen, G. Jezequel, G. Delhaye, B. Lepine, P. Turban, P. Schieffer, *Appl. Phys. Lett.* 100 (2012) 022103.
- ⁶³ L. Giordano, F. Cinquini, G. Pacchioni, *Phys. Rev. B* 73 (2005) 045414.
- ⁶⁴ U. Heiz, W. D. Schneider, *J. Phys.D:Appl. Phys.* 33 (2000) R85–R102.
- ⁶⁵ M. Sterrer, E. Fischbach, M. Heyde, N. Nilius, H.P. Rust, T. Risse, H.J. Freund, *J. Phys. Chem. B* 110 (2006) 8665.
- ⁶⁶ J. Kramer, W. Ernst, C. Tegenkamp, H. Pfnür, *Surf. Sci.* 517 (2002) 87.
- ⁶⁷ J. Kramer, C. Tegenkamp, H. Pfnür, *Phys. Rev. B* 67 (2003) 235401.
- ⁶⁸ T. Berger, M. Sterrer, O. Diwald, E. Knözinger, *J. Phys. Chem. B* 108 (2004) 7280.
- ⁶⁹ M. Sterrer, M. Heyde, M. Novicki, N. Nilius, T. Risse, H.P. Rust, G. Pacchioni, H.J. Freund, *J. Phys. Chem. B* 110 (2006) 46.
- ⁷⁰ V. Maurice, G. Despert, S. Zanna, M. P. Bacos, P. Marcus, *Nat. Mater.* 3 (2004) 687.
- ⁷¹ X. Shao, P. Myrach, N. Nilius, H. F. Freund, *J. Phys. Chem. C* 115 (2011) 8784.
- ⁷² S. Prada, L. Giordano, G. Pacchioni, *J. Phys. Chem. C* 117 (2013) 9943.
- ⁷³ C.G. Bond, D.T. Thompson, *Catal. Rev. Sci. Eng.* 41 (1999) 319.
- ⁷⁴ R. Meyer, C. Lemire, S.K. Shaikhutdinov, H.J. Freund, *Gold Bull.* 27 (2004) 72.
- ⁷⁵ G. J. Hutchings, M. Haruta, *Appl. Cat. A* 291 (2005) 2.
- ⁷⁶ D.T. Thompson, *Top. Catal.* 38 (2006) 231.
- ⁷⁷ M. Haruta, T. Kobayashi, H. Sano, N. Yamada, *Chem. Lett.* 16 (1987) 405.
- ⁷⁸ G. J. Hutchings, *J. Catal.* 96 (1985) 292.
- ⁷⁹ B. Nkosi, N. J. Coville, G. J. Hutchings, M. D. Adams, J. Friedl, F. Wagner, *J. Catal.* 128

- (1991) 366.
- ⁸⁰ T. Hayashi, K. Tanaka, M. Haruta, *J. Catal.* 178 (1998) 566.
- ⁸¹ M. Haruta, *Cattech* 6 (2002) 102, and references therein.
- ⁸² A. Corma, P. Serna, *Science* 313 (2006) 332.
- ⁸³ L. Prati, M. Rossi, *J. Catal.* 176 (1998) 552.
- ⁸⁴ B. Zope, D. D. Hibbitts and M. Neurock and R. J. Davis, *Science* 330 (2010) 74.
- ⁸⁵ D. Andreeva, *Gold Bull.* 35 (2002) 82.
- ⁸⁶ M. Valden, X. Lai, D.W. Goodman, *Science* 281 (1998) 1647.
- ⁸⁷ N. Lopez, J. K. Nørskov, *J. Am. Chem. Soc.* 124 (2002) 11262.
- ⁸⁸ A. Sanchez, S. Abbet, U. Heiz, W. Schneider, H. Häkkinen, R. Barnett, U. Landman, *J. Phys. Chem. A* 103 (1999) 9573.
- ⁸⁹ H. Häkkinen, S. Abbet, A. Sanchez, U. Heiz, U. Landman, *Angew. Chem. Int.* 42 (2003) 1297.
- ⁹⁰ Q. Fu, H. Saltsburg, M. Flytzani-Stephanopoulos, *Science* 301 (2003) 935.
- ⁹¹ M. Haruta, M. Date, *Appl. Catal. A* 222 (2001) 427.
- ⁹² M. Haruta, S. Tsubota, T. Kobayashi, H. Kageyama, N. Genet, B. Delmon, *J. Catal.* 144 (1993) 175.
- ⁹³ M. Turner, V. B. Golovko, O. P. H. Vaughan, P. Abdulkin, A. Bergenguer-Murcia, M. S. Tikhov, B. F. G. Johnson, R. M. Labert, *Nature* 454 (2008) 981–984.
- ⁹⁴ L. M. Molina, B. Hammer, *Phys. Rev. B* 69 (2004) 155424.
- ⁹⁵ B. Yoon, H. Häkkinen, U. Landman, A. Worz, J. Antonietti, S. Abbet, K. Judai, U. Heiz, *Science* 307 (2005) 403.
- ⁹⁶ S. Lee, C. Fang, T. Wu, S. L. Anderson, *J. Am. Chem. Soc.* 126 (2004) 5682.
- ⁹⁷ I. X. Green, W. Tang, M. Neurock, J. T. Yates, Jr, *Science* 335 (2011) 19336.
- ⁹⁸ L. Li, Y. Gao, H. Li, Y. Zhao, Y. Pei, Z. Chen, X. C. Zeng, *J. Am. Chem. Soc.* 135 (2013) 19336.
- ⁹⁹ I. N. Remediakis, N. Lopez, J.K. Nørskov, *Angew. Chem. Int* 44 (2005) 1824.
- ¹⁰⁰ I.N. Remediakis, N. Lopez, J.K. Nørskov, *Appl. Catal. A* 291 (2005) 13–20.
- ¹⁰¹ M. Sterrer, T. Risse, M. Heyde, H.P. Rust, H.J. Freund, *Phys.Rev. Lett.* 98 (2007) 206103.
- ¹⁰² P. Frondelius, A. Hellman, K. Honkala, H. Häkkinen, H. Grönbeck, *Phys. Rev. B* 78 (2008) 085426.
- ¹⁰³ R. Bader, *Atoms in Molecules*, Oxford University Press, 1990.

- ¹⁰⁴ G. Henkelman, A. Arnaldsson, H. Jónsson, *Comp. Mat. Sci.* 36 (2006) 354.
- ¹⁰⁵ V. Musolino, A. Selloni, R. Car, *J. Chem. Phys.* 108 (1998) 5044.
- ¹⁰⁶ C. J. Nelin, B. S Bagus, M. A. Brown, M. Sterrer, H.J. Freund, *Angw. Chem. Int. Ed* 50 (2011) 10174.
- ¹⁰⁷ D. Ricci, A. Bongiorno, G. Pacchioni, U. Landman, *Phys. Rev. Lett* 97 (2006) 036106.
- ¹⁰⁸ P. Frondelius, H. Häkkinen, K. Honkala, *Phys. Rev. B* 76 (2007) 073406.
- ¹⁰⁹ V. Simic-Milosevic, M. Heyde, X. Lin, T. Koenig, H. P. Rust, M. Sterrer, T. Risse, N. Nilius, H. J. Freund, L. Giordano, G. Pacchioni, *Phys. Rev. B* 78 (2008) 235429.
- ¹¹⁰ V. Simic-Milosevic, M. Heyde, N. Nilius, T. Konig, H. P. Rust, M. Sterrer, T. Risse, H. J. Freund, L. Giordano, G. Pacchioni, *J. Am. Chem. Soc* 130 (2008) 7814.
- ¹¹¹ P. Frondelius, H. Häkkinen, K. Honkala, *Phys. Chem. Chem. Phys.* 116 (2010) 4266.
- ¹¹² A. D. Vitto, G. Pacchioni, F. Delbecq, P. Sautet, *J. Phys. Chem. B* 109 (2005) 8040.
- ¹¹³ M. Walter, H. Häkkinen, *Phys. Rev. B* 72 (2005) 205440.
- ¹¹⁴ H. Häkkinen, U. Landman, *Phys. Rev. B* 62 (2000) R2287.
- ¹¹⁵ I. Yudanov, G. Pacchioni, K. Neyman, N. Rösch, *J. Phys. Chem. B* 101 (1997) 2786.
- ¹¹⁶ P. Frondelius, *Electronic, structural and chemical properties of gold clusters on ultra-thin oxide films*, Ph.D. thesis, University of Jyväskylä (2009).
- ¹¹⁷ N. Nilius, M. V. Ganduglia-Pirovano, V. Brazdova, M. Kulawik, J. Sauer, H.J. Freund, *Phys. Rev. Lett.* 100 (2008) 096802.
- ¹¹⁸ M. Walter, P. Frondelius, K. Honkala, H. Häkkinen, *Phys. Rev. Lett.* 99 (2007) 096102.
- ¹¹⁹ X. Lin, N. Nilius, H. Freund, M. Walter, P. Frondelius, K. Honkala, H. Häkkinen, *Phys. Rev. Lett.* 102 (2009) 20680.
- ¹²⁰ X. Lin, N. Nilius, M. Sterrer, P. Koskinen, H. Häkkinen, H. J. Freund, *Phys. Rev. B* 81 (2010) 153406.
- ¹²¹ C. Stiehler, Y. Pan, W. D. Schneider, P. Koskinen, H. Häkkinen, N. Nilius, H. J. Freund, *Phys. Rev. B* 88 (2013) 115415.
- ¹²² L. Giordano, G. Pacchioni, J. Goniakowski, N. Nilius, E. D. L. Rienks, H. J. Freund, *Phys. Rev. Lett.* 101 (2008) 026102.
- ¹²³ S. Siculo, L. Giordano, G. Pacchioni, *J. Phys. Chem. J* 113 (2009) 10256.
- ¹²⁴ P. Barbaro, C. Bianchini (Eds.), *Catalysis for Sustainable Energy Production*, Wiley-VCH, 2009.

- ¹²⁵ W. F. Schneider, *J. Phys. Chem* 108 (2004) 273.
- ¹²⁶ P. Broqvist, H. Grönbeck, *Surf. Sci.* 600 (2006) L214.
- ¹²⁷ H. Grönbeck, *J. Phys. Chem. B* 110 (2006) 11977.
- ¹²⁸ P. Broqvist, H. Grönbeck, *Surf. Sci.* 600 (2006) L214–L218.
- ¹²⁹ A. Gonchar, T. Risse, H.J. Freund, L. Giordano, C. D. Valentin, G. Pacchioni, *Angew. Chem. Int. Ed.* 50 (2011) 2635.
- ¹³⁰ A. Eichler, J. Hafner, *Phys. Rev. B* 59 (1999) 5960–5967.
- ¹³¹ B. Hammer, J.K. Nørskov, *Nature* 376 (1995) 238.
- ¹³² C. Harding, V. Habibpour, S. Kunz, A. N. S. Farnbacher, U. Heiz, U. Landman, *J. Am. Chem. Soc* 131 (2008) 538–548.
- ¹³³ L. M. Molina, B. Hammer, *J. Chem. Phys.* 123 (2005) 161104.
- ¹³⁴ B. Yoon, H. Häkkinen, U. Landman, *J. Phys. Chem. A* 107 (2003) 4066.
- ¹³⁵ L. Vilhelmsen, B. Hammer, *J. Chem. Phys.* 139 (2013) 204701.
- ¹³⁶ J. Nørskov, T. Bligaard, A. Logadottir, S. Bahn, L. Hansen, M. Bollinger, H. Bengaard, B. Hammer, Z. Sljivančanin, M. Mavrikakis, Y. Xu, S. Dahl, C. Jacobsen, *J. Catal.* 209 (2002) 275–278.
- ¹³⁷ K. Reuter, M. Scheffler, *Phys. Rev. B* 65 (2001) 035406.
- ¹³⁸ P. G. Jones, *Acta Crystallogr. Sect. B* 35 (1979) 1435.
- ¹³⁹ L. K. Ono, B. Roldan Cuenya, *J. Phys.Chem. C* 112 (2008) 4676.
- ¹⁴⁰ H. Shi, C. Stampfl, *Phys. Rev. B* 76 (2007) 075327.
- ¹⁴¹ X. Lin, B. Yang, H. M. Benia, P. Myrach, M. Yulikov, A. Aumer, M. A. Brown, M. Sterrer, O. Bondarchuk, E. Kieseritzky, J. Rucker, T. Risse, H. J. Gao, N. Nilius, H. J. Freund, *J. Am. Chem. Soc* 132 (2010) 7745.
- ¹⁴² M. A. Henderson, *Surf. Sci. Rep.* 46 (2002) 1–308.
- ¹⁴³ S. Kouva, J. Andersin, K. Honkala, J. Lehtonen, L. Lefferts, J. Kanervo, *Phys. Chem. Chem. Phys.* 16 (2014) 20650.
- ¹⁴⁴ W. Langel, M. Parrinello, *Phys. Rev. Lett.* 73 (1994) 504.
- ¹⁴⁵ W. Langel, M. Parrinello, *J. Chem. Phys.* 103 (1995) 3240.
- ¹⁴⁶ M. I. McCarthy, G. Schenter, C. A. Scamehorn, J. B. Nicholas, *J. Phys. Chem.* 100 (1996) 16989–16995.
- ¹⁴⁷ J. Carrasco, F. Illas, N. Lopez, *Phys. Rev. Lett.* 100 (2008) 016101.

- 148 K. Honkala, A. Hellman, H. Grönbeck, *J. Phys. Chem. C* 114 (2010) 7070.
- 149 R. S. Alvim, I. Borges, D. G. Costa, A. A. Leitao, *J. Phys. Chem. C* 116 (2012) 738.
- 150 L. Giordano, J. Goniakowski, J. Suzanne, *Phys. Rev. Lett.* 81 (1998) 1271.
- 151 M. Odelius, *Phys. Rev. Lett.* 82 (1999) 3919.
- 152 L. D. Site, A. Alavi, R. M. Bell, *J. Chem. Phys.* 113 (2000) 3344.
- 153 D. Ferry, S. Picaud, P. N. M. Hoang, C. Girardet, L. Giordano, B. Deirdjian, J. Suzanne, *Surf. Sci.* 409 (1998) 101.
- 154 Y. Yu, Q. Guo, S. Liu, E. Wang, P. J. Moller, *Phys. Rev. B* 68 (2003) 115414.
- 155 L. Savio, E. Celasco, L. Vattuone, M. Rocca, *J. Chem. Phys.* 119 (2003) 12053.
- 156 L. Savio, E. Celasco, L. Vattuone, M. Rocca, *J. Phys. Chem. B* 108 (2004) 7771.
- 157 S. Altieri, S. F. Contri, S. Valeri, *Phys. Rev. B* 76 (2007) 205413.
- 158 A. M. Ferrari, C. Roetti, C. Pisani, *Chem. Phys. Phys. Chem.* 9 (2007) 2350.
- 159 Z. Ding, S. Meng, *Phys. Rev. B* 86 (2012) 045455.
- 160 J. T. Newberg, D.E. Starr, S. Yamamoto, S. Kaya, T. Kendelewicz, E. R. Mysak, S. Porsgaard, M. B. Salmeron, G. E. Brown, A. Nilsson, H. Bluhm, *J. Phys. Chem. C* 115 (2011) 12864.
- 161 L. Giordano, A. M. Ferrari, *J. Phys. Chem. C* 116 (2013) 20349–20355.
- 162 J. Guo, X. Meng, J. Chen, J. Sheng, X. Z. Li, L. Xu, J. R. Shi, E. Wang, Y. Jiang, *Nat. Mat.* 13 (2014) 184.
- 163 U. Martinez, L. Giordano, G. Pacchioni, *J. Chem. Phys.* 128 (2008) 164707.
- 164 U. Martinez, J. F. Jerratsch, N. Nilius, L. Giordano, G. Pacchioni, H. J. Freund, *Phys. Rev. Lett.* 103 (2009) 056801.
- 165 R. Wlodarczyk, M. Sierka, J. Sauer, D. Löffler, J. J. Uhlrich, X. Yu, B. Yang, I. M. N. Groot, S. Shaikhutdinov, H. J. Freund, *Phys. Rev. B* 85 (2012) 085403.
- 166 T. Jaouen, S. Tricot, G. Delhaye, B. Lepine, D. S. G. Jezequel, P. Schieffer, *Phys. Rev. Lett.* 111 (2013) 027601.
- 167 J. Carrasco, N. Lopez, F. Illas, H. J. Freund, *J. Chem. Phys.* 125 (2006) 074711.
- 168 J. Jung, H. J. Shin, Y. Kim, M. Kawai, *J. Am. Chem. Soc.* 133 (2011) 6142.
- 169 L. Giordano, U. Martinez, G. Pacchioni, M. Watkins, A. L. Shluger, *J. Phys. Chem. C* 112 (2008) 3857.
- 170 J. Carrasco, N. Lopez, F. Illas, *Phys. Rev. Lett.* 93 (2004) 225502.
- 171 T. R. Munter, T. Bligaard, C. H. Christensen, J. K. Nørskov, *Phys. Chem. Chem. Phys.* 10

- (2008) 5202–5206.
- ¹⁷² P. Ferrin, D. Simonetti, S. Kandoi, E. Kunkes, J. A. Dumesic, J. K. Nørskov, M. Mavrikakis, *J. Am. Soc. Chem.* 131 (2009) 5809–5815.
- ¹⁷³ J. Andersin, N. Lopez, K. Honkala, *J. Phys. Chem. C* 113 (2009) 8278–8286.
- ¹⁷⁴ L. Nykänen, K. Honkala, *ACS Catal.* 3 (2013) 3026–3030.
- ¹⁷⁵ H. Falsig, B. Hvolbæk, I.S. Kristensen, T. Jiang, T. Bligaard, C.H. Christensen, J.K. Nørskov, *Angew. Chem. Int* 47 (2008) 4835.
- ¹⁷⁶ N. Lopez, J. Daniel Prades, F. Hernandez-Ramirez, J. R. Morante, J. Pan, S. Mathur, *Phys. Chem. Chem. Phys.* 12 (10) (2010) 2401–2406.
- ¹⁷⁷ Y. Cui, N. Nilius, H. J. Freund, S. Prada, L. Giordano, G. Pacchioni, *Phys. Rev. B* 88 (2013) 205421.
- ¹⁷⁸ A. R. West, *Basic Solid State Chemistry*, John Wiley & Sons, LTD, 2004.
- ¹⁷⁹ Y. Cui, X. Shao, M. Baldofski, J. Sauer, N. Nilius, H. J. Freund, *Ang. Chem. Int. Ed* 52 (2013) 11385.
- ¹⁸⁰ J. Nevalaita, H. Häkkinen, K. Honkala, to be submitted.
- ¹⁸¹ N. Mammen, S. Narasimhan, S. de Gironcoli, *J. Am. Chem. Soc.* 133 (2011) 2801–2803.